

Linear models of strip-type roughness

D. Lasagna^{1,†}, G. Zampino² and B. Ganapathisubramani¹

¹Aeronautics and Astronautics, Faculty of Engineering and Physical Sciences, University of Southampton, Hampshire SO17 1BJ, UK

²FLOW, Faculty of Engineering Mechanics, KTH Royal Institute of Technology, SE-100 44 Stockholm, Sweden

(Received 12 June 2024; revised 14 October 2024; accepted 18 November 2024)

Prandtl's secondary flows of the second kind generated by laterally varying roughness are studied using the linearised Reynolds-averaged Navier–Stokes approach proposed by Zampino *et al.* (*J. Fluid Mech.*, vol. 944, 2022, p. A4). The momentum equations are coupled to the Spalart–Allmaras model while the roughness is captured by adapting established strategies for homogeneous roughness to heterogeneous surfaces. Linearisation of the governing equations yields a framework that enables a rapid exploration of the parameter space associated with heterogeneous surfaces, in the limiting case of small spanwise variations of the roughness properties. Channel flow is considered, with longitudinal high- and low-roughness strips arranged symmetrically. By varying the strip width, it is found that linear mechanisms play a dominant role in determining the size and intensity of secondary flows. In this setting, secondary flows may be interpreted as the time-averaged output response of the turbulent mean flow subjected to a steady forcing produced by the wall heterogeneity. In fact, the linear model predicts that secondary flows are most intense when the strip width is about 0.7 times the half-channel height, in excellent agreement with available data. Furthermore, a unified framework to analyse combinations of heterogeneous roughness properties and laterally varying topographies, common in applications, is discussed. Noting that the framework assumes small spanwise variations of the surface properties, two separate secondary-flow-inducing source mechanisms are identified, i.e. the lateral variation of the virtual origin from which the turbulent structure develops and the lateral variation of the streamwise velocity slip, capturing the acceleration/deceleration perceived by the bulk flow over troughs and crests of non-planar topographies.

Key words: boundary layer structure, turbulent boundary layers, turbulence modelling

† Email address for correspondence: davide.lasagna@soton.ac.uk

1. Introduction

Prandtl's secondary flows of the second kind (Prandtl 1952) emerge when a turbulent flow develops over an heterogeneous surface with a lateral variation of its properties. Two equivalent standpoints, based on the analysis of the Reynolds-averaged equations, explain the formation of such currents. One standpoint considers secondary currents as the product of the imbalance between production and dissipation of turbulent kinetic energy induced by the roughness heterogeneity (Hinze 1973), whereby turbulence-rich fluid is advected towards low-turbulence regions. The second standpoint considers the streamwise vorticity balance (Perkins 1970), whereby cross-stream gradients of the Reynolds stresses arising from the cross-stream velocity components induce a turbulent torque that acts as a source term in the streamwise vorticity equation (Castro & Kim 2024). Overall, such mechanisms produce large-scale counter-rotating longitudinal rolls appearing in the time-averaged wall-bounded flow. The associated upwelling and downwelling motions produced by the rolls induce a lateral distortion of the boundary layer height (Barros & Christensen 2014), together with alternating high- and low-streamwise-momentum regions (Mejia-Alvarez & Christensen 2013; Willingham *et al.* 2014; Anderson *et al.* 2015), arranged analogously to the classical roll-streak pattern in shear flows (Brandt 2014).

Secondary flows are commonly observed in many industrial and environmental applications, where surfaces are either characterised by lateral variations of the topography, i.e. the elevation, or of the friction, e.g. by means of varying roughness properties. These two types of heterogeneity have been idealised in the literature as ridge-type and strip-type roughness configurations, respectively. The first type consists of longitudinal ribs located on a smooth, planar surface having rectangular or more complex cross-sections (Goldstein & Tuan 1998; Hwang & Lee 2018; Zampiron, Cameron & Nikora 2020; Castro *et al.* 2021; Long, Wang & Pan 2023; Zampino, Lasagna & Ganapathisubramani 2023; Zhdanov, Jelly & Busse 2024), or alternatively smooth sinusoidal modulations of the wall (Wang & Cheng 2006; Vidal *et al.* 2018). The second type, the focus of this work, consists of alternating longitudinal strips of high and low roughness. Secondary motions over such an arrangement have been extensively characterised experimentally (Bai *et al.* 2018; Wangsawijaya *et al.* 2020; Wangsawijaya & Hutchins 2022; Frohnäpfel *et al.* 2024), and in numerical simulations (Willingham *et al.* 2014; Anderson *et al.* 2015; Chung, Monty & Hutchins 2018; Forooghi, Yang & Abkar 2020; Stroh *et al.* 2020; Neuhauser *et al.* 2022; Schäfer *et al.* 2022).

Despite the burgeoning interest in these flows and the intense examination of their characteristics, there is a number of aspects clearly documented in the literature for which a physics-based, mechanistic model is not available. The first aspect is related to the marked dependence of the size and intensity of secondary flows on one or more spanwise length scales characterising the surface heterogeneity (Medjnoun, Vanderwel & Ganapathisubramani 2018; Yang & Anderson 2018; Wangsawijaya *et al.* 2020). For strip-type roughness this length scale is usually expressed by the width S of the strips. Consensus has emerged on the existence of three separate regimes as S varies in relation with the average boundary layer thickness δ (Chung *et al.* 2018). When the strip width is much smaller than the boundary layer thickness, $S \ll \delta$, secondary flows are confined to the vicinity of the surface and do not strongly influence the outer region. Conversely, when $S \gg \delta$ secondary flows are localised in regions where the surface properties vary more rapidly, and wide areas of local flow homogeneity are observed away from such regions (Wangsawijaya *et al.* 2020). When $S \approx \delta$, the secondary flows are most intense and can significantly influence the flow structure. Nevertheless, a model that captures the nature of these regimes and identifies boundaries between them is not available at present.

In addition, most studies have considered strips of equal width, but the width ratio between high- and low-roughness strips is certainly important, as it is for rectangular ridges where the ratio of recessed and elevated area influences the flow structure (Medjnoun, Vanderwel & Ganapathisubramani 2020; Zampino, Lasagna & Ganapathisubramani 2022).

A second aspect is related to the occurrence of the so-called tertiary flows. These are weaker longitudinal roll structures adjacent to the dominant rolls often associated to a reversal of the vertical flow direction at the centre of the high- (or low-)roughness strip, or at the centre of the ridge (or trough) (Vanderwel & Ganapathisubramani 2015). Tertiary flows are commonly observed over surfaces with longitudinal ridges (e.g. Medjnoun *et al.* 2020), especially when the width of the troughs or of the ridges is large enough to accommodate multiple streamwise vortices next to each other. For heterogeneous rough surfaces, however, tertiary flows have not been observed. In fact, for wide strips, cross-stream motions have been observed to be mostly confined in a roughly square region around the transition between the strips. This applies to both boundary layer (Wangsawijaya *et al.* 2020) and channel flows (Chung *et al.* 2018; Neuhauser *et al.* 2022). One explanation may be that tertiary flows over roughness strips might be difficult to discern in the mean flows obtained from experiments or simulations, especially when instantaneous structures meander quite significantly in the longitudinal direction (Kevin, Monty & Hutchins 2019; Zampiron, Cameron & Nikora 2021), smearing weak cross-stream motions. Neuhauser *et al.* (2022) hypothesised that the boundary conditions utilised in numerical simulations to capture the roughness effect may also play a role, although this hypothesis does not appear to explain why tertiary flows are not seen in experiments.

A third aspect that still lacks a robust mechanistic explanation is motivated by features of realistic surfaces in engineering and natural applications, whereby lateral changes of the roughness height are almost invariably accompanied by a lateral change in the elevation (Stroh *et al.* 2020; Schäfer *et al.* 2022). Decoupling these two effects may be easier in numerical simulations where the roughness heterogeneity is modelled by suitable spanwise heterogeneous boundary conditions applied to an otherwise planar boundary of the numerical domain (Chung *et al.* 2018; Neuhauser *et al.* 2022), but requires care when setting up experiments with, e.g. sandpaper strips or in roughness-resolving numerical simulations (Frohnappfel *et al.* 2024). One explicit attempt to study the coupling between these two effects was carried out by Stroh *et al.* (2020) and then later by Schäfer *et al.* (2022) who performed a series of direct numerical simulations over surfaces characterised by alternating rough and smooth regions. In their paper, Stroh *et al.* (2020) completely resolved the surface roughness using an immersed boundary method and studied three different configurations: the mean roughness height is (i) lower, (ii) equal to and (iii) higher than the elevation of the smooth surface. The authors observed a change in the flow organisation moving from case (i) to (iii) and *vice versa*. This behaviour was not reproduced in more recent roughness-resolving simulations (Frohnappfel *et al.* 2024), which was attributed to the importance of the strip width, relative to the roughness height.

One last aspect for which a model does not seem to be available concerns the relation between naturally occurring very-large-scale motions (VLSMs), populating the log-layer over homogeneous surfaces, and secondary flows (Chung *et al.* 2018; Lee, Sung & Adrian 2019; Wangsawijaya & Hutchins 2022). It has been speculated that secondary flows may be interpreted as VLSMs locked in place by the surface heterogeneity, given some similarity in their features. This can readily explain why secondary flows are most intense when $S \approx \delta$, because the strip width is commensurate with the spanwise length scale of such motions. Evidence shows that VLSMs and secondary flows do indeed coexist and do interact to a significant extent, since energy from the former appear to leak into the

latter (Wangsawijaya *et al.* 2020; Zampiron *et al.* 2020). However, the specific mechanism for which large-scale structures residing in the outer layer should be locked in place so effectively by the roughness heterogeneity is not fully clear.

In recent work (Zampino *et al.* 2022), we developed a predictive framework to understand how far can linear mechanisms go in explaining these aspects, focusing on ridge-type roughness. The framework originates from the long line of work that relies on the Reynolds-averaged Navier–Stokes (RANS) equations, augmented with a turbulent viscosity model and linearised about the turbulent mean, to explain the structure of smooth-wall turbulence (see del Álamo & Jiménez 2006; Pujals *et al.* 2009; Hwang & Cossu 2010; McKeon & Sharma 2010 and references therein), or as a systematic tool to investigate flow control strategies (Moarref & Jovanović 2012; Luhar, Sharma & McKeon 2015) and patterned surfaces (Chavarin & Luhar 2020; Ran, Zare & Jovanović 2020). Differently to previous efforts (Meyers, Ganapathisubramani & Cal 2019), the framework utilises the Spalart–Allmaras (SA) equation (Spalart & Allmaras 1994) to capture turbulent viscosity transport phenomena in combination with the nonlinear quadratic constitutive relation (QCR; see Spalart 2000) to model the anisotropy of the Reynolds stress tensor, required to produce secondary motions (see Speziale 1982; Speziale, Sarkar & Gatski 1991; Bottaro, Soueid & Galletti 2006). It also assumes that spanwise variations of the surface topography are infinitesimally small. This allows the mean response of the turbulent flow to be obtained using linear equations where different spanwise wavenumber components have decoupled. The relevance of the assumption for surfaces with finite-amplitude topographies remains to be examined, although recent work on rectangular ridges (Castro & Kim 2024) suggests that this approximation may only be acceptable for ridges with moderate height. This, in turn, indicates that the mean response of the turbulent flow to a perturbation of the surface topography may be quite nonlinear. Nevertheless, one advantage of the linear framework is its computationally efficiency. It thus enables the vast parameter space characterising heterogeneous surfaces to be explored rapidly, for instance to unravel the effect of ridge geometry (Zampino *et al.* 2023). A second key advantage of the framework is that it provides a perspective of secondary motions as being the output response of the turbulent mean subjected to a steady perturbation produced by the surface heterogeneity.

In this paper, we bring the same framework to bear on the problem of strip-type roughness. We assume that the spanwise variation of the roughness is small, so that linear equations governing the response of the flow can be obtained. The effect of the surface roughness is introduced following well-established modelling strategies for rough walls (Aupoix 2007; Prakash & Laurendeau 2020). Briefly, such strategies consist of modifying the virtual origin from which the turbulent flow develops, in order to obtain the desired shift of the logarithmic velocity profile. The overall aim of this paper is to characterise the formation and structure of secondary flows developing above strip-type roughness by means of the proposed linear framework. This will allow fundamental insight into the linear mechanisms that control such flows to be generated. We apply the proposed linear framework to flows in channels, and examine the role that the surface arrangement plays on: (i) the strength of secondary motions as a function of the strip width, identifying the three regimes discussed in Chung *et al.* (2018); (ii) the occurrence of tertiary flows as the relative width of the high- and low-roughness strips is varied; (iii) the structure of low- and high-momentum pathways; and, finally, (iv) the combination of roughness and surface elevation effects.

The modelling framework, and its extension to rough surfaces, is presented in § 2. Results are then reported in § 3. In § 4, the framework is generalised to more-complex

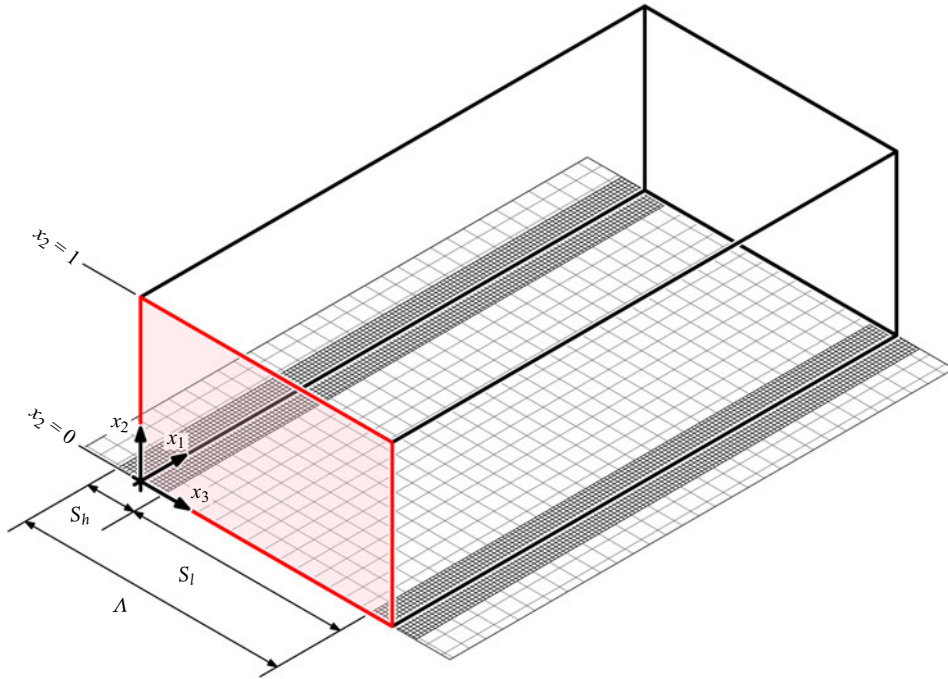


Figure 1. Sketch of the bottom half of the channel with high- and low-roughness strips, of width S_h and S_l , respectively, placed symmetrically on the bottom and upper (not shown) walls and aligned with the streamwise direction x_1 . This pattern repeats laterally with period $\Lambda = S_h + S_l$. These dimensions are normalised with the channel half-height h . The coordinate system is anchored at the bottom plane, at the centre of one of the high-roughness strips. Owing to the symmetry of the strip arrangement on the two walls, the shaded red area defines the fundamental repeating flow unit in which the flow structure is visualised later in the paper.

surface heterogeneities, combining the effects of roughness and surface elevation. Finally, conclusions are summarised in § 5.

2. Methodology

2.1. Governing equations

The incompressible flow of a fluid with kinematic viscosity ν and density ρ is considered in a pressure-driven channel with half-height h and subjected to a streamwise pressure gradient Π . The friction velocity $u_\tau = \sqrt{\tau_w/\rho}$, with $\tau_w = h\Pi$ the mean friction, yields the friction Reynolds number $Re_\tau = u_\tau h/\nu$. Index notation is used for the Cartesian coordinates x_i and velocities components u_i . Quantities are generally normalised by h and u_τ . The superscript $(\cdot)^+$ is omitted in the following to reduce clutter, unless necessary to identify a length scaled by the viscous length. The channel walls are covered by alternating strips of high and low roughness having width S_h and S_l , respectively, as shown in figure 1. The strips are aligned streamwise and are placed symmetrically on the two walls. The pattern repeats with spanwise periodicity $\Lambda = S_h + S_l$, the fundamental length scale. We also introduce the duty cycle $DC = S_h/\Lambda$ to characterise the relative width of the strips, and refer to S as the strip width when $S_h = S_l$, i.e. for $DC = 0.5$.

The continuity and momentum equations are Reynolds-averaged and made non-dimensional using h , u_τ and ρ . Average and fluctuation quantities are denoted by an overbar and a prime. For streamwise-aligned strips, we assume a streamwise-independent

time-averaged flow, i.e. $\partial(\cdot)/\partial x_1 \equiv 0$, which filters out the meandering of secondary currents (Zampiron *et al.* 2020). As a result, the mean pressure can be eliminated by considering the mean streamwise vorticity equation and introducing the streamfunction $\bar{\psi}$, satisfying $\nabla^2 \bar{\psi} = \bar{\omega}_1$ with

$$\bar{\omega}_1 = \frac{\partial \bar{u}_3}{\partial x_2} - \frac{\partial \bar{u}_2}{\partial x_3} \quad (2.1)$$

the mean streamwise vorticity. The cross-stream velocity components are $\bar{u}_2 = -\partial \bar{\psi} / \partial x_3$ and $\bar{u}_3 = \partial \bar{\psi} / \partial x_2$. The Reynolds-averaged equations for the streamwise momentum and the streamfunction are then

$$\frac{\partial \bar{\psi}}{\partial x_2} \frac{\partial \bar{u}_1}{\partial x_3} - \frac{\partial \bar{\psi}}{\partial x_3} \frac{\partial \bar{u}_1}{\partial x_2} = 1 + \frac{1}{Re_\tau} \left(\frac{\partial^2 \bar{u}_1}{\partial x_2^2} + \frac{\partial^2 \bar{u}_1}{\partial x_3^2} \right) + \frac{\partial \tau_{12}}{\partial x_2} + \frac{\partial \tau_{13}}{\partial x_3}, \quad (2.2a)$$

$$\begin{aligned} & \frac{\partial^2}{\partial x_2 \partial x_3} \left[\left(\frac{\partial \bar{\psi}}{\partial x_2} \right)^2 - \left(\frac{\partial \bar{\psi}}{\partial x_3} \right)^2 \right] + \left(\frac{\partial^2}{\partial x_3^2} - \frac{\partial^2}{\partial x_2^2} \right) \frac{\partial \bar{\psi}}{\partial x_2} \frac{\partial \bar{\psi}}{\partial x_3} \\ &= \frac{1}{Re_\tau} \left(\frac{\partial^2}{\partial x_2^2} + \frac{\partial^2}{\partial x_3^2} \right)^2 \bar{\psi} + \frac{\partial^2}{\partial x_2 \partial x_3} (\tau_{33} - \tau_{22}) + \left(\frac{\partial^2}{\partial x_2^2} - \frac{\partial^2}{\partial x_3^2} \right) \tau_{23}, \end{aligned} \quad (2.2b)$$

where $\tau_{ij} = -\overline{u'_i u'_j}$ is the Reynolds stress tensor.

2.2. Turbulence modelling

When the linear Boussinesq hypothesis is used to express the deviatoric component of the Reynolds stresses as a function of the mean velocity gradients, namely

$$\tau_{ij}^L = 2\nu_t S_{ij}, \quad (2.3)$$

where ν_t is the turbulent eddy viscosity and S_{ij} is the symmetric component of the mean velocity gradient tensor

$$S_{ij} = \frac{1}{2} \left(\frac{\partial \bar{u}_i}{\partial x_j} + \frac{\partial \bar{u}_j}{\partial x_i} \right), \quad (2.4)$$

the Reynolds stresses in (2.2b) do not depend on the streamwise velocity. Then, the streamfunction equation decouples from the streamwise momentum equation and its solution is trivially $\bar{\psi} \equiv 0$, i.e. no secondary flows are generated.

As discussed extensively in the literature (see e.g. Perkins 1970; Speziale 1982; Bottaro *et al.* 2006), a nonlinear stress model is needed to predict Prandtl's secondary flows of the second kind, produced by spatial gradients of the anisotropy of the Reynolds stresses. Several approaches have been proposed in literature (e.g. Speziale 1982; Chen, Lien & Leschziner 1997). Here we utilise the QCR nonlinear model presented in Spalart (2000), whereby the deviatoric component of the Reynolds stresses becomes

$$\tau_{ij}^Q = \tau_{ij}^L - c_{r1} [O_{ik} \tau_{jk}^L + O_{jk} \tau_{ik}^L], \quad (2.5)$$

where O_{ij} is the normalised rotation tensor defined as

$$O_{ij} = 2W_{ij} / \sqrt{\frac{\partial \bar{u}_m}{\partial x_n} \frac{\partial \bar{u}_m}{\partial x_n}}, \quad (2.6)$$

and W_{ij} is the antisymmetric part of the velocity gradient tensor, with m and n being summation indices. The QCR model depends on a tuning single constant, whose value

$c_{r1} = 0.3$ was calibrated to match the anisotropy of the outer region of wall-bounded turbulent flows in Spalart (2000). The default value is used throughout the paper.

To close the momentum equations, a model for the eddy viscosity ν_t is necessary. Previous studies that have utilised the linearised Navier–Stokes equations have adopted analytical eddy viscosity profiles to analyse smooth-wall turbulent flows (see del Álamo & Jiménez 2006; Pujals *et al.* 2009; Hwang & Cossu 2010; Morra *et al.* 2019 among others). Here, a complete transport model is preferred over such analytical ansätze, as it is not clear *a priori* how the eddy viscosity field should change when the mean flow structure is significantly distorted by secondary currents, or when roughness effects are important. For this purpose, the SA turbulence model (Spalart & Allmaras 1994) is employed in this work. The SA model is preferred here over other commonly employed two-equation models because it can be linearised relatively easily. In addition, the SA model was developed for attached shear flows, hence it should provide satisfactory predictions for the present case. The steady SA model defines a transport equation for the modified eddy viscosity $\tilde{\nu}$, normalised with u_τ and h . This quantity is related to the turbulent viscosity by the relation

$$\nu_t = \tilde{\nu} f_{v1}, \quad (2.7)$$

where $f_{v1} = \chi^3 / (\chi^3 + c_{v1}^3)$ with $\chi = Re_\tau \tilde{\nu}$ and c_{v1} a tuning constant. The modified eddy viscosity coincides with the turbulent viscosity away from the wall. The term f_{v1} ensures the correct decay of the turbulent viscosity in the viscous sublayer (Herring & Mellor 1968; Spalart & Allmaras 1994), although $\tilde{\nu}$ behaves linearly in the log layer down to the wall, which is advantageous for numerical reasons. The transport equation is

$$\bar{u}_i \frac{\partial \tilde{\nu}}{\partial x_i} = c_{b1} \tilde{S} \tilde{\nu} + \frac{1}{\sigma} \left\{ \frac{\partial}{\partial x_j} \left[\left(\frac{1}{Re_\tau} + \tilde{\nu} \right) \frac{\partial \tilde{\nu}}{\partial x_j} \right] + c_{b2} \frac{\partial \tilde{\nu}}{\partial x_j} \frac{\partial \tilde{\nu}}{\partial x_j} \right\} - c_{w1} f_w \left(\frac{\tilde{\nu}}{d} \right)^2, \quad (2.8)$$

where the terms model advection, production, diffusion and destruction, respectively. In the production term, the quantity \tilde{S} is defined as

$$\tilde{S} = \sqrt{2W_{ij}W_{ij}} + \frac{\tilde{\nu}}{\kappa^2 d^2} f_{v2} \quad \text{with} \quad f_{v2} = 1 - \frac{\chi}{1 + \chi f_{v1}}, \quad (2.9)$$

with κ the von Kármán constant. The destruction term in (2.8) captures the blocking effect of the wall on turbulent fluctuations and is a function of the distance to the nearest surface d . With this term, the model produces an accurate log-layer in wall-bounded flows. It includes a non-dimensional function f_w that increases the decay of the destruction term in the outer region. This term reads as

$$f_w = g \left[\frac{1 + c_{w3}^6}{g^6 + c_{w3}^6} \right]^{1/6}, \quad (2.10)$$

with

$$g = r + c_{w2}(r^6 - r) \quad \text{and} \quad r = \frac{\tilde{\nu}}{\tilde{S} \kappa^2 d^2}. \quad (2.11a,b)$$

Standard values for the calibration constants $c_{v1} = 7.1$, $c_{b1} = 0.1355$, $\sigma = 2/3$, $c_{b2} = 0.622$, $c_{w2} = 0.3$ and $c_{w3} = 2$ are used (Spalart & Allmaras 1994), with $c_{w1} = c_{b1}/\kappa^2 + (1 + c_{b2})/\sigma$ to balance production, diffusion and destruction in the log-layer, with $\kappa = 0.41$.

2.3. Roughness model for homogeneous surfaces

Many rough-wall modelling strategies for homogeneous roughness for RANS simulations rely on the notion of equivalent sandgrain roughness k_s^+ (e.g. Durbin *et al.* 2000; Suga, Craft & Iacovides 2006; Aupoix 2007; Brereton & Yuan 2018; Prakash & Laurendeau 2020, among others). These strategies, described in this section, link the equivalent sandgrain roughness to suitable non-zero turbulence quantities (the modified eddy viscosity for the SA model) at the smooth, planar boundary of the numerical domain, to capture the increased turbulence activity near the rough surface and obtain the desired shift of the logarithmic velocity profile as the main effect of the surface roughness. No-slip boundary conditions are applied for the velocity. The mean turbulence structure is assumed to develop from a new virtual origin, displaced beneath the numerical boundary by a suitable distance d_0^+ , to be determined (Rotta 1962). Relying on the outer-layer similarity hypothesis of Townsend (1976), far away from the surface the law of the wall is preserved, and the shift of the streamwise velocity profile observed over a rough surface is captured by the empirical relation

$$\left. \frac{\partial \bar{u}_{1,r}}{\partial x_2^+} \right|_{x_2^+} = \left. \frac{\partial \bar{u}_{1,s}}{\partial x_2^+} \right|_{x_2^+ + d_0^+}, \quad (2.12)$$

where the subscripts $(\cdot)_r$ and $(\cdot)_s$ denote quantities over the rough and smooth walls. Integrating this relation from the wall with $\bar{u}_{1,r}(x_2^+ = 0) = 0$ yields

$$\bar{u}_{1,r}(x_2^+) = \bar{u}_{1,s}(x_2^+ + d_0^+) - \bar{u}_{1,s}(d_0^+), \quad (2.13)$$

which evaluated far away from the surface gives the logarithmic shift

$$\Delta \bar{u}_1 = \bar{u}_{1,r}(x_2^+ \gg d_0^+) - \bar{u}_{1,s}(x_2^+ \gg d_0^+) = \bar{u}_{1,s}(d_0^+), \quad (2.14)$$

i.e. the distance d_0^+ can be found as the wall-normal coordinate where the velocity over the smooth wall is equal to the desired velocity shift $\Delta \bar{u}_1$.

Then a roughness function that links the equivalent sandgrain roughness to the shift of the log region is required. Among various options available, here we use the Colebrook–Grigson roughness function (Grigson 1992), given by

$$\Delta \bar{u}_1 = \frac{1}{\kappa} \log \left(1 + \frac{k_s^+}{\exp(3.25\kappa)} \right), \quad (2.15)$$

with κ being the von Kármán constant. Although significant variations can be observed in the transitional regime, little practical difference are found for the fully rough regime in using this and other models, such as Nikuradze's roughness function (Aupoix 2007). Knowing the smooth-wall velocity profile $\bar{u}_{1,s}(x_2^+)$ and equating the relations (2.15) and (2.14) allows the displacement d_0^+ to be expressed as a function of the desired sandgrain roughness k_s^+ .

With such information, a solution consistent with (2.12) can be found when the eddy viscosity satisfies

$$\nu_{t,r}(x_2^+) = \nu_{t,s}(x_2^+ + d_0^+). \quad (2.16)$$

This is achieved in two steps. First, the inhomogeneous boundary condition

$$\tilde{\nu}_r(x_2^+ = 0) = \tilde{\nu}_s(d_0^+) = d_0^+ \kappa / Re_\tau \quad (2.17)$$

is enforced to the modified eddy viscosity in the SA model, where the second equality stems from the fact that, in the SA model, $\tilde{\nu}$ varies linearly as κx_2 near the wall by

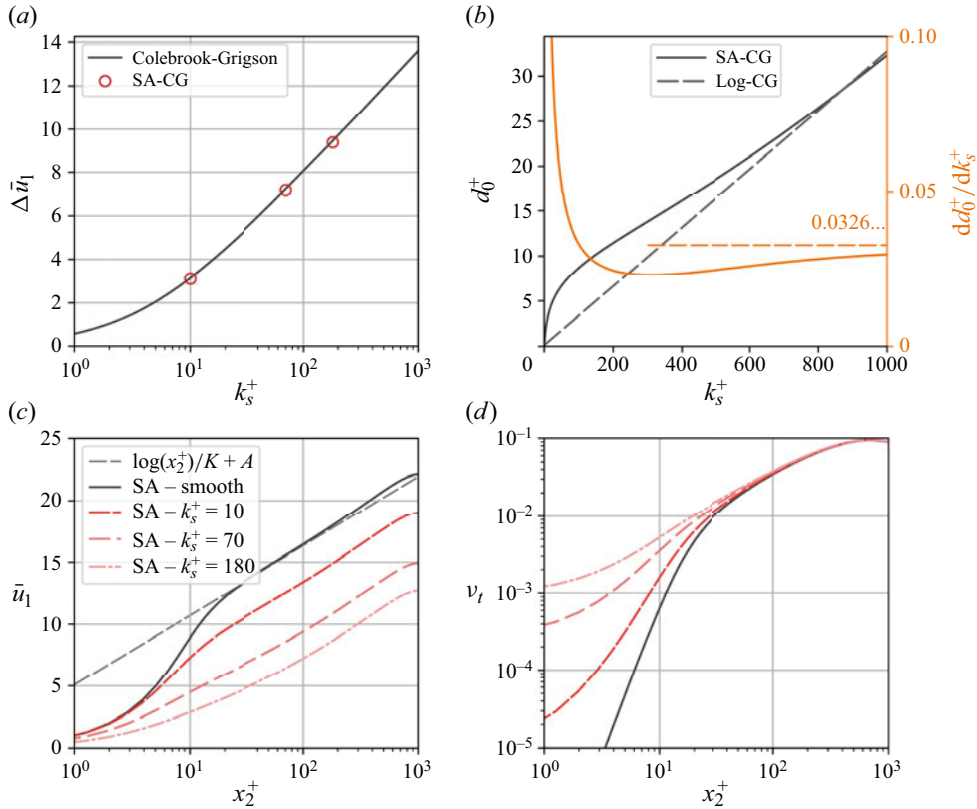


Figure 2. (a) The analytical Colebrook–Grigson roughness function (solid line) and the logarithmic shift obtained via the procedure described in the text (open circles). (b) Virtual origin d_0^+ as a function of the equivalent sandgrain roughness k_s^+ obtained by using the smooth-wall SA velocity profile or the standard log-law (black lines). The orange lines denote the derivative of d_0^+ with respect to k_s^+ (axes on the right-hand side). Numerical solutions of the streamwise momentum equation and the SA turbulence model for channels with smooth and homogeneous rough walls for $Re_\tau = 1000$. (c) Streamwise velocity. (d) Turbulent viscosity. The circles in panel (a) indicate the logarithmic shift associated to the profiles of panel (c), calculated using the procedure in the text. For the logarithmic law, the constants $\kappa = 0.41$ and $A = 5.1$ are used.

construction. Second, the distance d between any point in the computational domain and the nearest wall appearing in the SA model, as a fundamental field variable that controls the balance between the production and destruction terms, needs to be updated to reflect the location of the new virtual origin, slightly below the numerical domain boundary. For instance, for the lower half of the channel, $d = x_2 + d_0$. Overall, this procedure allows the SA model to produce the desired shifted logarithmic velocity profile, consistent with the updated boundary condition (2.17) on the modified eddy viscosity.

Figure 2 illustrates example results at $Re_\tau = 1000$, at which most of the results presented in later sections were obtained. Solutions were obtained numerically with an in-house RANS code, based on a Chebyshev-collocation discretisation method. Mesh independence studies, omitted here, showed that 252 collocation points were sufficient to obtain mesh-independent results. The nonlinear system of algebraic equations formed by the streamwise momentum equation and the SA equation was solved using a Jacobian-free Newton–Krylov technique (Knoll & Keyes 2004), using the ‘hookstep’ approach of Viswanath (2007) to improve convergence. Initial guesses for the streamwise velocity were

obtained by first solving the momentum equation using Cess's analytical eddy viscosity profile (Reynolds & Hussain 1972). For a desired equivalent sandgrain roughness k_s^+ for the homogeneous surface, the Colebrook–Grigson roughness function in figure 2(a) is first used to obtain $\Delta\bar{u}_1$. Using the smooth-wall velocity profile obtained from the SA model (figure 2c), the virtual origin d_0^+ is obtained upon applying (2.14) (figure 2b). Repeating this procedure for several equivalent sandgrain roughness yields the curve ‘SA-CG’ in figure 2(b). Clearly, the choice of the smooth-wall velocity profile influences the results. For instance, coupling the Colebrook–Grigson formula to the log-law $\bar{u}_{1,s}(x_2^+) = \log(x_2^+)/\kappa + A$, with $\kappa = 0.41$ for consistency with the standard SA model and $A = 5.1$, yields

$$d_0^+ = \left(1 + \frac{k_s^+}{\exp(3.25\kappa)}\right) \exp(-\kappa A) \simeq 0.0326k_s^+, \quad (2.18)$$

denoted as ‘Log-CG’ in the figure. This virtual origin is then used for the boundary condition (2.17) and in the SA model. Overall, this yields shifted velocity profiles (figure 2c), that produce the desired $\Delta\bar{u}_1$ as a function of k_s^+ . This is demonstrated in figure 2(a), which compares the Colebrook–Grigson roughness function (solid line) used at the first step with the logarithmic shift obtained at the last step of this procedure for three values of k_s^+ , denoted by the circles. It is worth pointing out that small absolute variations of the turbulent viscosity distribution in figure 2(d) are sufficient to produce relatively significant alterations of the mean velocity profile. Numerically, this makes the equations relatively stiff to solve.

2.4. Roughness model for heterogeneous surfaces

The equivalent sandgrain roughness is a dynamic parameter that is non-trivially related to the roughness geometry. For homogeneous roughness, it can be readily estimated from correlations once the shift of the velocity profile is known. However, for heterogeneous roughness, e.g. the present surface with alternating strips, it is not immediately clear how one should assign an equivalent sandgrain roughness to the two strips from velocity measurements, as the flow structure and, thus, the logarithmic shift also depend on the spatial distribution of the roughness properties (Wangsawijaya *et al.* 2020). This conundrum is fundamentally the same as discussed in numerical simulation studies in which the roughness is not resolved but suitable boundary conditions are applied at the smooth, planar boundary of the numerical domain. In such strategies, the roughness heterogeneity can be modelled directly by a lateral variation of the shear stress (Chung *et al.* 2018) or by a lateral variation of the transversal slip length (Neuhauser *et al.* 2022). These strategies require a model that links the boundary conditions to the desired logarithmic shift. Such models are generally derived for homogeneous surfaces and their applicability to heterogeneous surfaces may be questioned.

Here, given the lack of a better strategy, the aforementioned approach is adopted. Specifically, the alternating strips are defined by a spanwise variation of the equivalent sandgrain roughness, following the expression

$$k_s^+(x_3) = k_s^{(0)} + \epsilon k_s^{(1)}(x_3), \quad (2.19)$$

where $k_s^{(0)}$ is the reference, spatially constant roughness height and $k_s^{(1)}(x_3)$ captures the variation of the roughness properties over the two strips. For a unitary $k_s^{(1)}$ amplitude of the roughness pattern, the spanwise variation is defined by the unitary peak-to-peak amplitude,

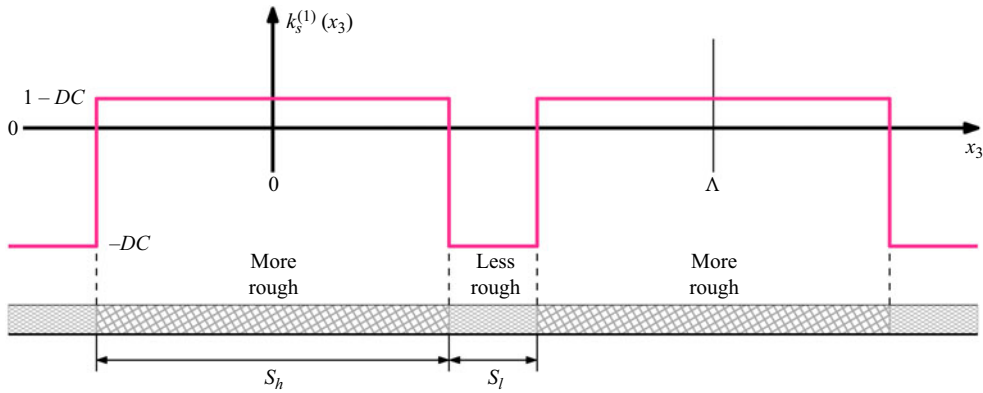


Figure 3. The hashed diagram on the bottom shows the heterogeneous rough surface with roughness strips having higher or lower roughness than average, covering about two periods of the laterally repeating pattern. The duty cycle is 0.8. The diagram at the top shows the distribution of the perturbation roughness height $k_s^{(1)}(x_3)$. Note that this term represents the deviation from the reference roughness height $k_s^{(0)}(x_3)$, as defined by (2.19).

zero-mean function

$$k_s^{(1)}(x_3) = \begin{cases} 1 - DC & 0 \leq x_3 \leq S_h/2 \text{ and } \Lambda - S_h/2 \leq x_3 \leq \Lambda \\ -DC & S_h/2 \leq x_3 \leq \Lambda - S_h/2, \end{cases} \quad (2.20)$$

as demonstrated in figure 3. Because the difference in roughness between the two strips defined by $k_s^{(1)}(x_3)$ is unitary, the parameter ϵ in (2.19) controls the actual difference in roughness between the two strips, although it is not related to the physical structure of the roughness. This definition is preferred over specifying the roughness of the two strips, or considering roughness strips separated by smooth regions (Wangsawijaya *et al.* 2020). This choice is motivated by the fact that we consider in the present analysis the asymptotic limit when ϵ tends to zero, so that linearised equations governing the response of the turbulent shear flow developing over a rough surface to a small spanwise variation of the roughness properties can be obtained.

2.5. Linearisation of the Reynolds-averaged equations and of the roughness model

The streamwise momentum, streamfunction and SA equations form a coupled system of three nonlinear partial differential equations that can be solved for any desired strip configuration. However, when the difference between the properties of the high- and low-roughness strips is small, in the limit when $\epsilon \ll 1$, the resulting flow structure can be thought of as the sum of the flow in a channel with the homogeneous reference roughness $k_s^{(0)}$ and a small perturbation, produced by the surface roughness heterogeneity $k_s^{(1)}(x_3)$ and capturing the heterogeneous flow structure of secondary flows. This small perturbation obeys a set of linear equations which is much easier to solve, and only captures linear input–output mechanisms. To derive such equations, a generic time-averaged flow quantity $\bar{q}(x_2, x_3)$ is first expanded in series as

$$\bar{q}(x_2, x_3) = q^{(0)}(x_2) + \epsilon q^{(1)}(x_2, x_3) + O(\epsilon^2). \quad (2.21)$$

Higher-order terms in (2.21) are neglected within the current framework. The convergence of the series for finite ϵ and the validity of the resulting predictions must still be verified.

However, this approach is motivated by the goal of calculating the linear response of the turbulent mean flow to a small, nearly infinitesimal, perturbation in surface attributes, to assess how well linear mechanisms can account for the formation of secondary structures over heterogeneous surfaces.

Substituting this expression for all mean quantities in the Reynolds-averaged equations and in the SA equation, and taking terms at order zero in ϵ , leads to the nonlinear equations governing the flow over the homogeneous rough surface. The streamwise vorticity equation is trivially satisfied by $\psi^{(0)} = 0$. The streamwise momentum equation is

$$0 = 1 + \frac{1}{Re_\tau} \frac{\partial^2 u_1^{(0)}}{\partial x_2^2} + \frac{\partial \tau_{12}^{(0)}}{\partial x_2}, \quad (2.22)$$

and it is coupled to the SA transport equation via the definition of the Reynolds stress $\tau_{12}^{(0)}$. These two equations are solved in a coupled fashion using the approach discussed in § 2.3. At first order, the equations governing the perturbation of the streamwise velocity and the streamfunction are

$$-\frac{\partial \psi^{(1)}}{\partial x_3} \Gamma = \frac{1}{Re_\tau} \left(\frac{\partial^2}{\partial x_2^2} + \frac{\partial^2}{\partial x_3^2} \right) u_1^{(1)} + \frac{\partial \tau_{12}^{(1)}}{\partial x_2} + \frac{\partial \tau_{13}^{(1)}}{\partial x_3}, \quad (2.23a)$$

$$0 = \frac{1}{Re_\tau} \left(\frac{\partial^2}{\partial x_2^2} + \frac{\partial^2}{\partial x_3^2} \right)^2 \psi^{(1)} + \frac{\partial^2}{\partial x_2 \partial x_3} (\tau_{33}^{(1)} - \tau_{22}^{(1)}) + \left(\frac{\partial^2}{\partial x_2^2} - \frac{\partial^2}{\partial x_3^2} \right) \tau_{23}^{(1)}, \quad (2.23b)$$

where we define $\Gamma = \partial u_1^{(0)} / \partial x_2$, showing that the zero-order solution, through the mean velocity gradient Γ , needs to be available for the solution of the first-order equations. The first term on the left-hand side of (2.23a), analogous to the off-diagonal coupling operator in the Orr–Sommerfeld–Squire linearised equations, is the only coupling term explicitly appearing in this set of equations. Physically, this term captures the interaction between the mean shear and the perturbation velocity and underpins energy extraction mechanisms in shear flows via the lift-up effect (Brandt 2014). All other terms obtained from the nonlinearity vanish because the streamfunction at order zero is identically zero. Secondary currents also introduce an alteration of the spatial organisation of the turbulent viscosity through an alteration of the balance of the transport terms in the SA equation. The linearised SA equation governing such organisation is coupled to the streamwise momentum and the streamfunction equations and contributes to the perturbation of the Reynolds stresses entering (2.23). Linearisation of the SA model is tedious and leads to complex expressions. More detail on the linearisation procedure is reported in our previous work (see Appendix B of Zampino *et al.* (2022)), and is omitted here for brevity.

It is worth noting that the streamfunction equation contains the perturbation of the Reynolds stresses originating from the cross-stream velocity components, as is well known (Perkins 1970). Although at order zero these terms exhibit negligible influence, at order one the perturbation of the Reynolds stress tensor becomes pivotal to couple the two equations in the differential system (2.23). Here, the first-order stresses are found by expanding the nonlinear Reynolds stress model (2.5) in a Taylor series in ϵ , leading to

$$\tau_{ij}^{(1)} = \tau_{ij}^{L(1)} - c_{r1} [O_{ik}^{(1)} \tau_{jk}^{L(0)} + O_{ik}^{(0)} \tau_{jk}^{L(1)} + O_{jk}^{(1)} \tau_{ik}^{L(0)} + O_{jk}^{(0)} \tau_{ik}^{L(1)}], \quad (2.24)$$

where $O_{ij}^{(1)}$ is the normalised rotation tensor induced by the first-order velocity components (see Appendix A). Developing (2.24), the individual perturbation Reynolds stresses

appearing in (2.23) are

$$\tau_{12}^{(1)} = v_t^{(0)} \frac{\partial u_1^{(1)}}{\partial x_2} + v_t^{(1)} \Gamma + 2c_{r1} \text{sign}(\Gamma) v_t^{(0)} \frac{\partial^2 \psi^{(1)}}{\partial x_2 \partial x_3}, \quad (2.25a)$$

$$\tau_{13}^{(1)} = v_t^{(0)} \frac{\partial u_1^{(1)}}{\partial x_3} - 2c_{r1} \text{sign}(\Gamma) v_t^{(0)} \frac{\partial^2 \psi^{(1)}}{\partial x_2^2}, \quad (2.25b)$$

$$\tau_{23}^{(1)} = v_t^{(0)} \left(\frac{\partial^2}{\partial x_2^2} - \frac{\partial^2}{\partial x_3^2} \right) \psi^{(1)} + 2c_{r1} \text{sign}(\Gamma) v_t^{(0)} \frac{\partial u_1^{(1)}}{\partial x_3}, \quad (2.25c)$$

$$\tau_{22}^{(1)} = -2v_t^{(0)} \frac{\partial^2 \psi^{(1)}}{\partial x_2 \partial x_3} + 2c_{r1} \left[\text{sign}(\Gamma) v_t^{(0)} \frac{\partial u_1^{(1)}}{\partial x_2} + \text{sign}(\Gamma) v_t^{(1)} \Gamma \right], \quad (2.25d)$$

$$\tau_{33}^{(1)} = 2v_t^{(0)} \frac{\partial^2 \psi^{(1)}}{\partial x_2 \partial x_3}. \quad (2.25e)$$

Except for $\tau_{33}^{(1)}$, which coincides with its linear Boussinesq's definition, all other stresses contain an additional term specific to the QCR model and proportional to the c_{r1} constant. In particular, the stresses appearing in the streamfunction equation contain spatial gradients of the streamwise velocity, and *vice versa*. These terms result in a tighter, two-way coupling between the streamfunction and streamwise velocity equations, now able to sustain secondary currents.

To obtain boundary conditions for the field variables, the wall roughness treatment model discussed in § 2.4 needs to be linearised. The key idea is that small spanwise perturbations of the equivalent sandgrain roughness are modelled as small spanwise variations of the virtual origin. More formally, over the heterogeneous surface given by (2.19), the shift of the virtual origin varies according to

$$d_0^+(x_3) = d_0^{(0)} + \epsilon d_0^{(1)}(x_3), \quad (2.26)$$

where $d_0^{(0)}$ is the shift of the virtual origin of the reference homogeneous surface with equivalent sandgrain roughness $k_s^{(0)}$. On the other hand, the first-order term can be found by differentiating numerically the curve reported in figure 2(b) at $k_s^+ = k_s^{(0)}$ and using (2.20), since

$$d_0^{(1)} = \left. \frac{dd_0^+}{dk_s^+} \right|_{k_s^{(0)}} k_s^{(1)}. \quad (2.27)$$

Asymptotically, for large $k_s^{(0)}$ and considering the log law, the derivative of the curve in figure 2(b) tends to about 0.0326, implying that a peak-to-peak variation of the equivalent sandgrain roughness of $1/0.0326 \approx 30$ is necessary to obtain a peak-to-peak variation of the virtual origin equal to the viscous length scale. Once $d_0^{(1)}$ is known, linearising (2.17) yields the wall condition for the modified eddy viscosity

$$\tilde{v}^{(1)}(x_2 = 0) = d_0^{(1)} \kappa / Re_\tau, \quad (2.28)$$

showing that the spanwise variation of the roughness properties is modelled as a lateral change in the eddy viscosity at boundary of the numerical domain. Finally, homogeneous boundary conditions are used for the streamwise velocity perturbation and the streamfunction perturbation and its wall-normal derivative.

One last remark is in order. A sensible question is whether the inclusion of the linearised turbulence model to describe the perturbation of the turbulent viscosity is really necessary, given that this is not customary in many previous studies using linearised Navier–Stokes equations. On the one hand, the strength of the mean flow response to a lateral perturbation of the surface attributes may likely depend on the well-known selective amplification properties of the linearised Navier–Stokes operator, which are largest when such perturbation occurs at a specific spanwise length scale. On the other hand, the SA model provides a means to model realistically the effect of the surface heterogeneity, because it provides clear insight into how the perturbation of the effective distance d influences the perturbation of the turbulent viscosity field. As described in § 4, the lateral perturbation of the distance d is the dominant source mechanism that leads to secondary flows in the present framework. In principle, one could first introduce an ansatz on the perturbation of the turbulent viscosity and then only solve the linearised Navier–Stokes equations. However, given the range of transport phenomena modelled by the SA equation, defining the correct ansatz does not appear to be a straightforward task.

2.6. Numerical solution of the linearised equation

The spanwise variation of the equivalent roughness height can be modelled as a square wave approximated by the cosine series

$$k_s^{(1)} = \sum_{n=1}^{\infty} k_s^n \cos\left(n \frac{2\pi}{\Lambda} x_3\right). \quad (2.29)$$

The coefficients k_s^n can be calculated analytically for each combination of widths S_h and S_l and the corresponding coefficients d_0^n for the spanwise variation of the virtual origin $d_0^{(1)}$ are found by using (2.27).

Expanding the unknown field variables at first order in series, e.g. for the streamwise velocity

$$u_1^{(1)}(x_2, x_3) = \sum_{n=1}^{\infty} \hat{u}_1(x_2; n) \cos\left(n \frac{2\pi}{\Lambda} x_3\right), \quad (2.30)$$

and substituting these expressions in the linearised equations leads to one set of three linear ordinary differential equations in x_2 for each integer wavenumber. As opposed to previous studies considering the linearised Navier–Stokes equations (Chavarin & Luhar 2020; Ran *et al.* 2020), each set of three ordinary differential equations is independent of all other wavenumbers and can be solved in isolation. This would not be the case if higher-order terms had been retained in (2.21), and a larger problem would need to be solved taking into account harmonic interactions. A Chebyshev-collocation method was used for the discretisation. Although the field variable d in the SA model has a sharp cusp at $x_2 = 0$ and, hence, a spectral technique is not ideal for the solution of this problem, we have observed that the numerical method is robust enough to provide accurate results when a sufficiently fine grid is used. In the following simulations, we used up to 252 collocation points. For the spanwise discretisation, we observed that solutions converge relatively rapidly with the number of Fourier modes retained in the expansion (2.29). This can be motivated by the observation that, far away from the wall, only large-scale perturbations of the surface features can influence the flow structure, while the effect of small-scale perturbations, i.e. sharp gradients of the boundary conditions (Neuhauser *et al.* 2022), decays more rapidly with the distance from the wall (Meyers *et al.* 2019). The

number of spanwise modes required increases with the fundamental wavelength Λ . We always checked that results did not change visibly when doubling the number of modes. As a reference, 20 modes were sufficient at $\Lambda \approx 1$ to obtain a converged description of the perturbation velocity field.

The final solution is then found by combining the solutions at each wavenumber, as the superposition principle applies. One important implication of this property is that the flow structure over surfaces with complex topographic/roughness characteristics (Mejia-Alvarez & Christensen 2013; Barros & Christensen 2014) may be rationalised and better understood by decomposing the surface forcing into its constitutive components. The strength of the mean flow response at each spanwise length scale will then depend on the amplitude of such components times a factor that captures the selective amplification properties of the linearised Navier–Stokes operator (Chernyshenko & Baig 2005), augmented by the linearised SA equation.

It is worth noting that the spatially constant component at $n = 0$ does not appear in (2.29) because of the assumption that the spanwise variation of the roughness height given by (2.20) is zero mean. It does also not appear in the solution (2.30), because the linearity of the model implies that a perturbation of the surface properties at wavenumber n only produces a distortion of the time-averaged flow at the same wavenumber. A corollary of this property is that the present model does not predict any change in mean friction drag, the subject of several recent studies (Hutchins *et al.* 2023; Frohnafel *et al.* 2024). In fact, the spanwise-constant component $\hat{u}_1(x_2; 0)$ and, thus, the perturbation of the bulk velocity computed from this profile, which would allow calculating the change in friction coefficient at constant friction velocity, is identically zero. The model does indeed capture the spanwise modulation of the streamwise velocity distribution, i.e. high- and low-momentum pathways (Barros & Christensen 2014), but second-order effects in ϵ that produce interactions between harmonics are necessary to obtain a velocity perturbation at wavenumber $n = 0$ from surface perturbations at $n > 1$ and, thus, capture the change in friction (Zampino 2023).

3. Structure and strength of secondary currents

The volume-averaged kinetic energy of the cross-sectional velocity components \mathcal{K} , defined as

$$\mathcal{K} = \frac{1}{4\Lambda} \int_0^2 \int_0^\Lambda [u_2^{(1)}(x_2, x_3)^2 + u_3^{(1)}(x_2, x_3)^2] dx_3 dx_2, \quad (3.1)$$

is used here to characterise the strength of the secondary flows. We also use the streamfunction peak $\max_{x_2, x_3} |\psi^{(1)}(x_2, x_3)|$ to quantify the cross-stream flow rate associated with the vortices, as in other studies (Vidal *et al.* 2018). Note that these variables are scaled with u_τ and h . The solution of the linearised equations for a given strip configuration can be obtained quite rapidly, which enables a rapid exploration of the parameter space (S_h, S_l). Results are reported in figure 4(a,b) for $Re_\tau = 1000$, and using $k_s^{(0)} = 180$. Figure 4(c,d) shows cuts along lines for three duty cycles as a function of the fundamental length scale Λ .

We note that, as in our previous application of these techniques to surfaces with longitudinal ridges (Zampino *et al.* 2022), the results of the linearised model become asymptotically Reynolds number independent for high Reynolds numbers, somewhat supporting the weak Reynolds number dependence documented in the literature (Wangsawijaya & Hutchins 2022). This ultimately stems from known properties of the SA model (Spalart & Allmaras 1994), which is designed to produce an eddy viscosity

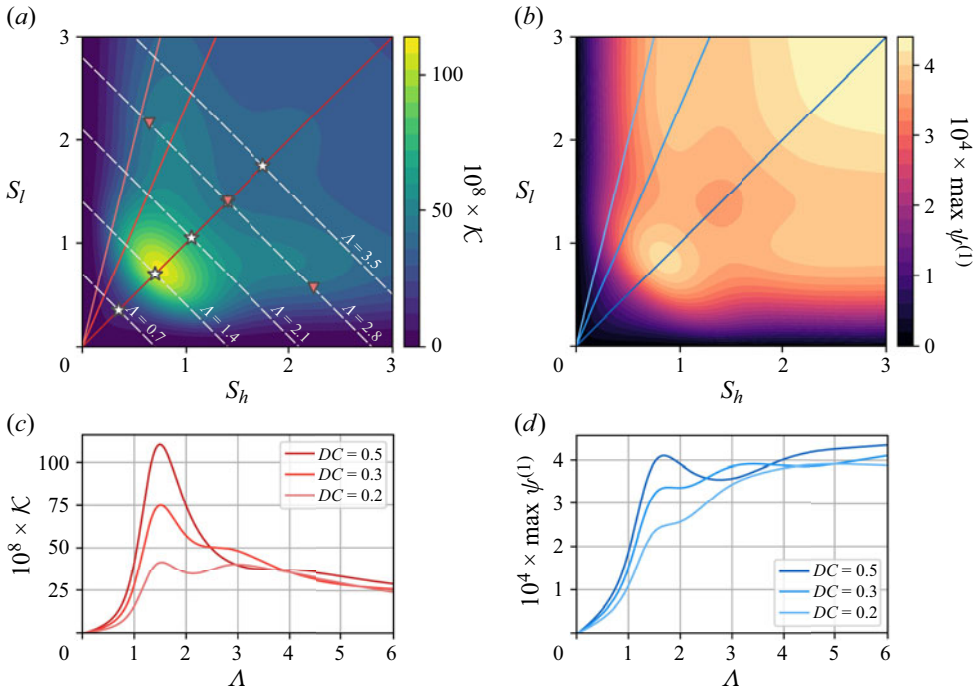


Figure 4. Contours of the volume-averaged kinetic energy of the cross-stream velocities \mathcal{K} (a) and the streamfunction peak value $\max_{x_2, x_3} |\psi^{(1)}|$ (b) as a function of the width of the high- and low-roughness strips. The Reynolds number is $Re_\tau = 1000$ and $k_s^{(0)} = 180$. Cases at constant spatial fundamental length scale Λ are identified by the dashed diagonal lines with negative slope. Markers identify cases discussed later in the text. (c,d) The same two quantities for $DC = 0.2, 0.3$ and 0.5 , as a function of Λ .

distribution consistent with the log law. Hence, the discussion presented here can also be applied to higher-Reynolds number-flows relevant to applications. Note also that flow variables, such as the velocity or streamfunction perturbations, are computed in the present linear modelling framework per unit variation of the equivalent sandgrain roughness height $k_s^{(1)}$ (scaled in inner units) in analogy to what was described for ridge-type roughness in Zampino *et al.* (2022) where the same quantities are obtained per unitary ridge height (scaled in outer units). Given that experiments on secondary flows over heterogeneous surfaces are often conducted on roughness strips with a considerable difference in roughness properties (Chung *et al.* 2018; Wangsawijaya *et al.* 2020), the numerical values reported here will appear quite small. For graphical convenience, quantities are pre-multiplied by a large factor, e.g. 10^8 in figure 4(a), in the figures.

Regardless of the quantity used for measuring the strength of the secondary currents, a peak is observed for $S_h = S_l \simeq 0.7$, corresponding to a fundamental length scale $\Lambda \approx 1.4$, although the streamfunction peaks slightly later. Further, the quantities in figure 4 are symmetric with respect to the line $DC = 0.5$, where the strength peaks. For $\Lambda \gtrsim 2.5$ two peaks are observed, located symmetrically with respect to the line $DC = 0.5$. Examination of the flow structure for some of these cases indicates that the secondary flows observed over the high- and low-roughness regions for a generic configuration (S_h, S_l) are identical in strength but opposite in flow direction when the width of the two strips is swapped. The strip width at which secondary currents are most intense reflects previous observations. For instance, Chung *et al.* (2018), using large-eddy simulations, and Wangsawijaya *et al.*

(2020), using experiments above spanwise-alternating smooth and rough strips, reported a maximum intensity for the secondary flows when the width of the strips is comparable with the boundary layer thickness. In particular, Wangsawijaya *et al.* (2020) found that the swirl strength was largest among the cases they considered for $S_h = S_l = 0.62$.

The contours of the kinetic energy around the peak region appear elongated along the line $S_h + S_l = \text{const.}$ As a result, the three cuts along lines at constant duty cycle all display a peak for $\Lambda \simeq 1.4$, which may be interpreted as Λ being the relevant length scale. This is partly correct, as the response to sinusoidal perturbations of the sandgrain roughness does indeed peak for this length scale, as for ridge-type roughness (Zampino *et al.* 2022). However, there is a marked effect of the relative size of the strips away from the peak and the two widths are indeed necessary to correctly characterise the response. The maps of figure 4 show strong similarities with the maps displayed in Zampino *et al.* (2022, see figure 10) and Zampino *et al.* (2023) (see figure 2) for the ridge-type roughness, as the peak amplification occurs for similar values of Λ . This similarity suggests that the selective amplification of secondary flows is an intrinsic property of the mean flow, and perhaps less strongly an effect of the type of forcing, e.g. whether it is produced by elevation (ridges) or roughness (strips) variations. In this regard, there has been recent discussion on the relation and coexistence between secondary currents and VLSMs (e.g. Lee *et al.* 2019). One speculation is that secondary currents are naturally occurring VLSMs that are phase locked spatially by the heterogeneous surface (Chung *et al.* 2018; Wangsawijaya *et al.* 2020) and emerge in the time-averaged flow. The present approach, based on the Reynolds-averaged equations where the concept of VLSMs does not apply immediately, suggests that secondary currents may be interpreted as the time-averaged response of a forcing localised near the wall and produced by gradients of the turbulent stresses. The linearised Navier–Stokes operator with its selective amplification properties then produces more intense time-averaged structures at specific forcings wavelengths, when $\Lambda \simeq 1.4$. This hypothesis leverages the same physics used in transient growth analysis studies (del Álamo & Jiménez 2006; Cossu, Pujals & Depardon 2009; Pujals *et al.* 2009) to explain the formation of coherent structures in shear flows from properties of the Orr–Sommerfeld–Squire equations, except that here we consider the steady response to a given steady perturbation localised at the wall rather than the transient amplification of an optimal initial perturbation.

3.1. Flow structure

To visualise the cross-stream structure of the secondary currents, fields of the wall-normal and spanwise velocity perturbation are reported in figure 5, for duty cycle $DC = 0.5$, i.e. for equal length of the high- and low-roughness strips, for a range of strip widths S . These configurations correspond to the star markers in figure 4(a). Contour lines of the streamfunction are also reported. The roughness strips produce two counter-rotating vortices inducing a downwelling over the high-roughness regions and an upwelling over the low-roughness regions. For narrow strips, even narrower than what shown here, the vortices are confined in the near-wall region and the flow appears homogeneous at distances from the wall larger than the strip width. Increasing the strip width, the vortices grow with S until they occupy the full half-height of the channel. For $S \simeq 0.7$, the cross-stream components and, in particular, the wall-normal component is more intense than all other cases considered. This configuration identifies the peak amplification region of the maps of figure 4. Increasing S further, the strength of the wall-normal motions decreases slightly, but the volume-averaged strength of such motions decreases much further as the flow structure converges to an idealised wide-strip asymptotic limit where

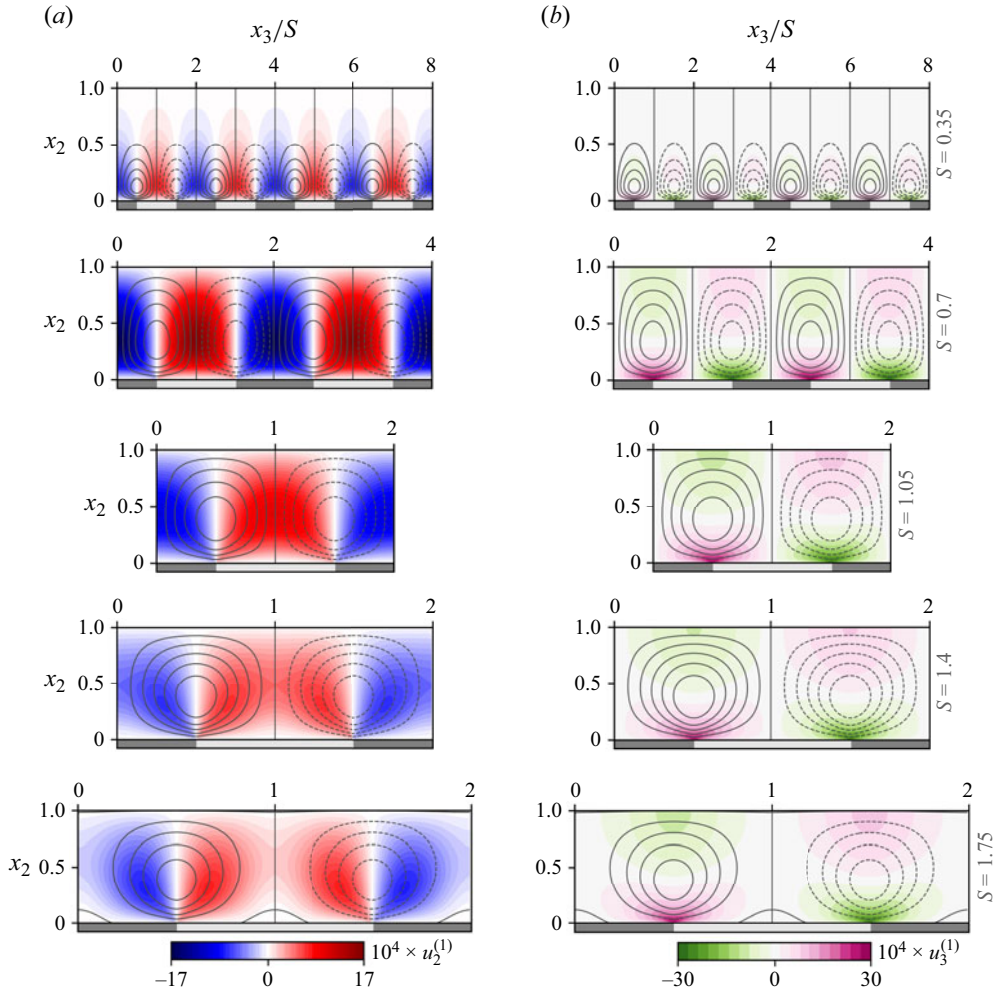


Figure 5. Colour maps of the wall-normal velocity perturbation $u_2^{(1)}$ over roughness strips at $DC = 0.5$ for several strip widths S (a). The field in the fundamental domain (see figure 1) is repeated four and two times for the two narrowest strip cases. Contour lines of the perturbation of the streamfunction $\psi^{(1)}$ are also reported to better describe the secondary flows. Negative $\psi^{(1)}$ are indicated by using dashed lines. Contours of the spanwise velocity perturbation $u_3^{(1)}$ (b). The Reynolds number is $Re_\tau = 1000$, for $k_s^{(0)} = 180$. The darker/lighter patches denote the high/low roughness strips.

moderately intense cross-stream motions are only found in the immediate vicinity of the transition between strips, with fluid is at rest in the ‘homogeneous’ regions above the centres of the roughness strips. This explains the trend of the two quantities in figure 4(c,d). While \mathcal{K} is a volume-averaged quantity and decreases with S for $S \gg 1$, the streamfunction peak is a local quantity that measures the strength of the individual vortex cores. This quantity shows a first peak for $S \simeq 0.75$, and eventually tends to an asymptotic value (with a larger amplitude) for large S , characterising the strength of the ‘isolated vortex’ regime.

Near the transition between strips, the spanwise component is particularly intense in the near-wall region (figure 5b). The spanwise velocity peak is more intense than the vertical velocity peak in agreement with observations Frohnäpfel *et al.* (2024), and is localised in the near-wall region. Given that the spanwise velocity obeys no-slip condition, this results

in very high streamwise vorticity localised at the transition between strips. Analyses not reported here show that the wall-normal location of the spanwise velocity peak scales in inner units when the Reynolds number is increased, while its magnitude becomes Re_τ independent.

From a qualitative viewpoint, the flow structure predicted by the present linearised model resembles previous experimental observations (Wangsawijaya *et al.* 2020) and numerical simulations (Chung *et al.* 2018; Neuhauser *et al.* 2022). One aspect of discussion concerns the spanwise location of the streamwise-aligned vortices with respect to the alternating pattern of roughness. In the present case, the vortices are symmetrically located above the interface between the strips. This is because the linearity of the governing equations preserves the symmetry that exists across the jump. By contrast, the experiments of Wangsawijaya *et al.* (2020) show that the centres of the vortices are typically found over the low-roughness region. The same was predicted by the simulations of Chung *et al.* (2018), using an inhomogeneous shear-stress boundary condition to model the roughness. The puzzling aspect is that one would initially attribute the displacement of the vortices to nonlinear convective effects not captured by the linear model, as if the vortices were transported towards the low-roughness region by the relatively intense spanwise velocities near the wall associated to the streamwise vorticity field. However, such a displacement is not observed in the simulations of Neuhauser *et al.* (2022) who applied a Navier slip boundary condition for the spanwise velocity to model the roughness, or occurs in the opposite direction in more-recent roughness-resolving simulations of submerged roughness strips (Frohnepfel *et al.* 2024).

From a quantitative viewpoint, a comparison with published results is slightly less straightforward given the particular set-up considered in this paper. For this purpose, we use the channel-flow simulations of Chung *et al.* (2018), at $Re_\tau = 590$. The roughness strips are modelled by setting the shear stress to 50 % more and 50 % less than the average shear stress. Assuming that the low- and high-roughness strips correspond to the smooth and rough wall regions, respectively, Chung *et al.* (2018) estimates that the equivalent sandgrain roughness of the roughness patches is $k_s^+ = 205$. With such settings, they observe maximum wall-normal velocities that peak between $0.3u_\tau$ and $0.4u_\tau$ (see their figure 9a). To match the roughness properties of these simulations, one needs to recall that the solution produced by the present linear model is defined per unit variation of the equivalent sandgrain roughness between the strips. From the results of figure 5, maximum velocities on the order of $17 \times 10^{-4}u_\tau$ are obtained, for the optimal width S . Multiplying this value by $k_s^+ = 205$ we obtain velocities on the order of $0.35u_\tau$, in very good quantitative agreement with the numerical simulations. Given that the intensity of the cross-stream velocity components characterises somehow the equilibrium between source and sink mechanisms of the streamwise vorticity balance (Stroh *et al.* 2016; Castro & Kim 2024), the favourable agreement with simulations suggests that such mechanisms are correctly captured by the linearised RANS model. However, the maximum wall-normal velocity in Chung *et al.* (2018) is obtained for a relatively wide strip, $S = 1.57$, while the present model indicates that the peak occurs at $S \approx 0.7$, and lower velocities are observed for $S = 1.57$. It is argued that this is not a Reynolds number effect, but it is due to the vortices in Chung *et al.* (2018) being, as discussed, closer to each other than the strip width S would suggest, resulting in larger induced velocities. Evidence for this is given by the fact that the wall-normal velocities depend on the duty cycle DC , as shown later in figure 9, and peak when the vortices are artificially pushed together by a narrow low-roughness strip, $S_L < S_h$.

3.2. High- and low-momentum pathways

A unique characteristic of flows over heterogeneous surfaces is that the longitudinal secondary currents are flanked by high- and low-momentum regions, produced by the vertical ‘pumping’ of high- and low-momentum fluid, respectively, induced by the vortical motions (Mejia-Alvarez & Christensen 2013; Barros & Christensen 2014; Willingham *et al.* 2014), which determine a significant spanwise alteration of the boundary layer depth. Although a wall-bounded flow above an homogeneous rough surface displays a positive deficit of the streamwise velocity due to the flow deceleration induced by the surface roughness (Jiménez 2004), the colocation between the high- and low-momentum regions and the roughness strips is counterintuitive as faster flow can be found for certain conditions above the high-roughness strips. In this section, we demonstrate that the present framework clearly captures this phenomenon.

In figure 6, contours of the streamwise velocity perturbation $u_1^{(1)}$ are shown for the same configurations of figure 5. This visualisation differs to what customarily reported in previous work in that it shows the *velocity deviation* from the streamwise velocity distribution $u_1^{(0)}$ observed over the homogeneous surface. The difference between the maps in the two columns is that in figure 6(a) the secondary currents were artificially ‘turned off’ by setting the constant c_{r1} in the nonlinear stress model to zero, so that spanwise and wall-normal gradients of the mean streamwise velocity do not produce any of the Reynolds stresses in the streamwise vorticity equation necessary to sustain longitudinal vortices. In figure 6(b), solutions for the standard value $c_{r1} = 0.3$ are reported. Without secondary currents, the flow experiences a net deceleration above the high-roughness strips, especially in the near-wall region. However, further away from the wall, e.g. at the centre of the channel, the change in streamwise velocity depends strongly on the strip width, because this parameter controls the depth at which the roughness-induced deceleration ‘diffuses’ in the shear flow from the wall due to the turbulent viscosity field. For narrow strips, the velocity deficit at the channel centre is small, and only becomes significant when the strip width is at least half the half-height of the channel. When secondary currents are ‘turned back on’ (figure 6b), the streamwise velocity over the high-roughness strips is now generally positive because of the downwelling motion in this region, and *vice versa* for the low-roughness strips. This only applies for $x_2 \gtrsim 0.1$, because nearer to the wall the local roughness properties control whether the flow is faster/slower. These motions produce dispersive stresses, e.g. $u_1^{(0)} u_2^{(0)}$, that alter the equilibrium in the streamwise direction and result in a non-trivial dependence of the streamwise velocity from the wall. This, fundamentally, implies that the logarithmic velocity distribution is significantly altered by the addition of the dispersive stresses. However, as the strips become wider, secondary currents are not intense enough to produce any significant alteration of the streamwise momentum equilibrium and the deceleration effect produced by the high roughness begins to dominate, starting from the region closest to the wall. Overall, this is the same behaviour observed experimentally (Wangsawijaya *et al.* 2020; Frohnepfel *et al.* 2024), where a downwards/upwards bulging of the contours of the streamwise velocity are observed at the edge of the boundary layer/near the wall.

The influence of the strip width on the perturbation of the streamwise velocity field is summarised in figure 7. The streamwise velocity profile at the centre of the high-roughness strip is extracted from several calculations with S in the range $[0.1, 20]$, with and without the nonlinear Reynolds stress model. These profiles are concatenated together to form the maps in figures 7(a) and 7(b), respectively. For the case with $c_{r1} = 0.3$, we also report a similar plot for the wall-normal component, in figure 7(c). Given that a logarithmic

Linear models of strip-type roughness

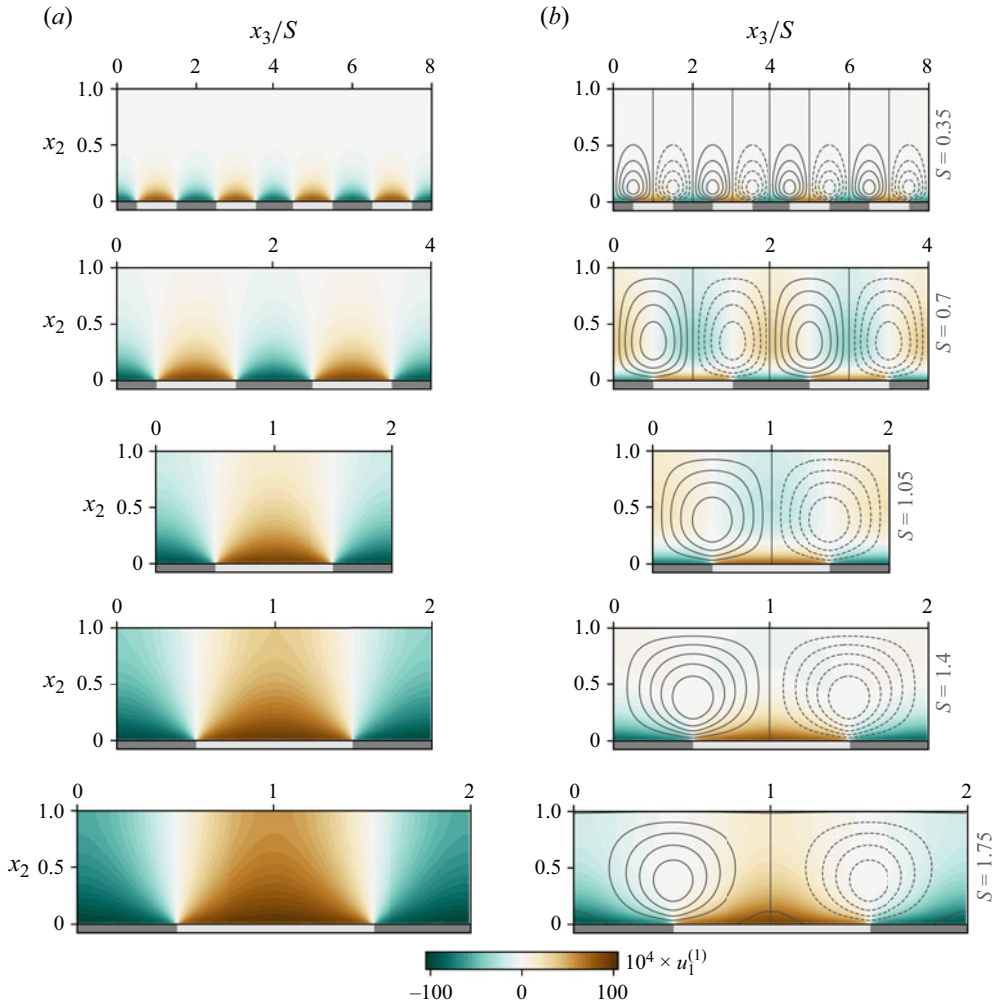


Figure 6. Contours of the streamwise velocity perturbation $u_1^{(1)}$ over roughness strips at $DC = 0.5$ for several strip widths S , without QCR model (a) and with QCR model (b). The field in the fundamental domain (see figure 1) is repeated four and two times for the two narrowest strip cases. Contour lines of the perturbation of the streamfunction $\psi^{(1)}$ are also reported to visualise the secondary flows. Negative $\psi^{(1)}$ contours are indicated by dashed lines. The Reynolds number is $Re_\tau = 1000$, for $k_s^{(0)} = 180$. The darker/lighter patches denote the location of the high-/low-roughness strips.

velocity shift is not a meaningful quantity to compute, we report in figure 7(d) the velocity deviation in the centre of the channel, above the centre of the high-roughness strips. In figure 7(c), the solid red line denotes the wall-normal location of the perturbation streamfunction peak. The three regimes discussed in Chung *et al.* (2018) can be clearly identified. For wide strips, the velocity deficit tends to a value controlled by the roughness function at $k_s^{(0)}$ for both cases, as the turbulent structure over each strip tends to its equivalent over an homogeneous surface given that the influence of neighbouring patches and of the secondary currents localised at the transition between strips vanishes. In this regime, the model predicts that the centre of the rolls is located at a distance from the wall of about 0.42, i.e. the rolls are space-filling in the vertical direction. The streamwise

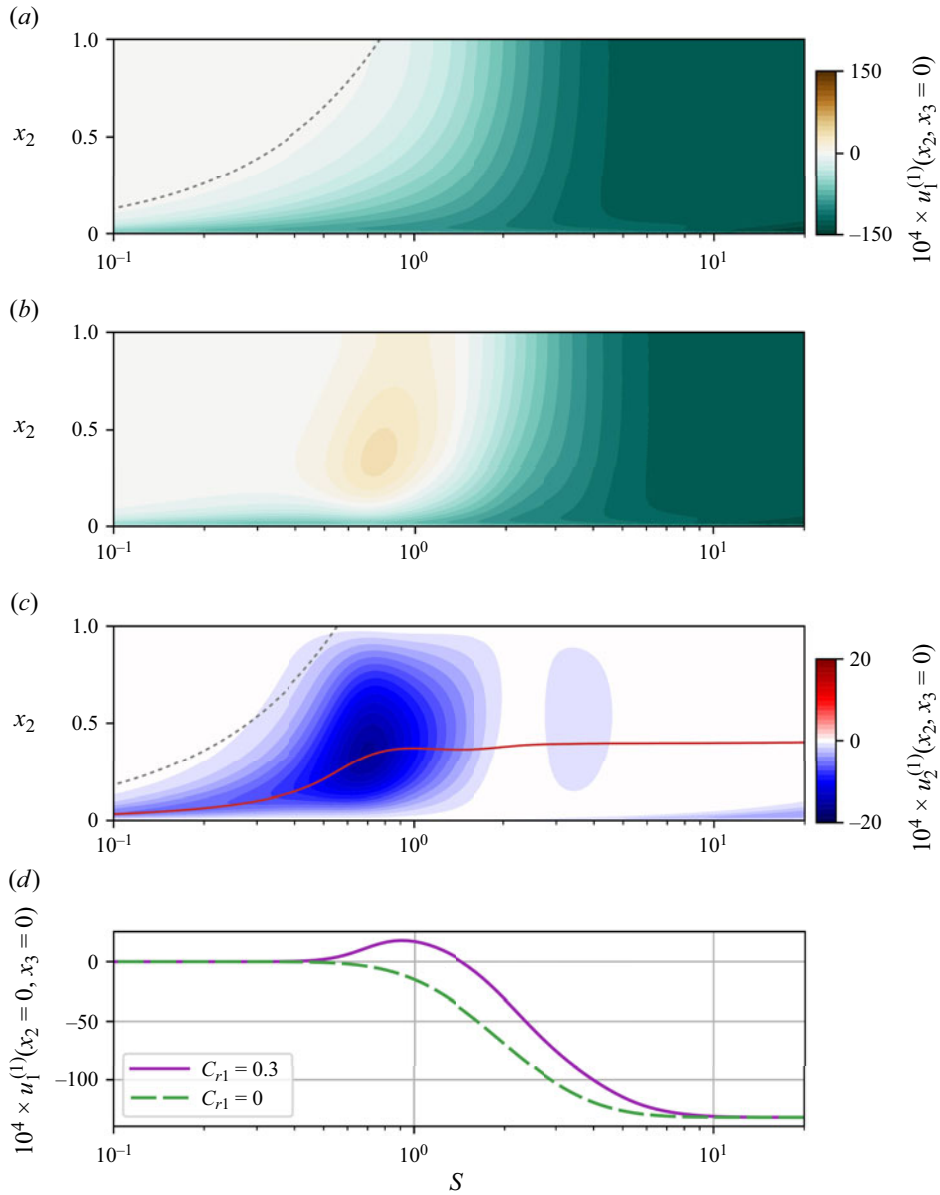


Figure 7. Streamwise velocity extracted on a vertical line at the centre of the high-roughness strip for increasing strip width S , for $c_{r1} = 0$ (a) and the standard value 0.3 (b). Wall-normal velocity extracted on the same vertical line for $c_{r1} = 0.3$ (c). The dashed lines indicate wall-normal distances growing linearly with S for $DC = 0.5$. Streamwise velocity perturbation above the centre of the high-roughness strip, at the mid-plane, for the same two cases as a function of the strip width (d). The Reynolds number is $Re_\tau = 1000$ and $k_s^{(0)} = 180$.

velocity perturbation is also roughly constant as a function of the distance from the wall for $S \gtrsim 8$, producing the expected shift of the logarithmic velocity profile over each strip, regardless of whether the nonlinear Reynolds stress is active or not.

For narrow strips, the height of the channel is much larger than the ‘depth’ at which the effect of the wall inhomogeneity is perceived, analogously to the blending height

concept for spatially varying roughness discussed in (Bou-Zeid, Parlange & Meneveau 2007). For the case $c_{r1} = 0$, without rolls, this depth (estimated from the contours of the streamwise velocity perturbation) varies linearly with S , as one would expect to see in a diffusion-driven problem, given that the turbulent viscosity does not vary significantly except for near the wall. For the case $c_{r1} = 0.3$, with rolls, the depth measured in terms of the wall-normal velocity also appears to increase linearly with S , at least for the smallest S analysed here. However, the linear scaling (the dashed lines) appears to lose accuracy relatively rapidly, at $S \approx 0.25$, as soon as the rolls occupy about half of the half-channel height. In between these two regimes, in the ‘transitional regime’ of Yang & Anderson (2018), the streamwise velocity perturbation display a complex behaviour, highlighting the significant lack of flow homogeneity. At $S = 0.7$ the rolls are most intense and induce the maximum perturbation at a wall-normal location close to the centres of the rolls. However, the velocity perturbation reaches its peak at the mid-plane only at $S = 0.95$ and then changes sign from $S \gtrsim 1.75$. Interestingly, the model never predicts flow reversal when the strip width is increased, in agreement with observations in the literature (Neuhauser *et al.* 2022).

Overall, the present framework appears to capture the three flow regimes documented in the literature correctly. The implication is that linear mechanisms, whereby secondary flows may be interpreted as the output response of the mean shear flow to a steady forcing localised at the wall, may be sufficient to predict the size and strength of the rolls. Based on the streamwise velocity evaluated at the mid-plane, the boundaries may be located at $S \approx 0.4$ and $S \approx 8$, but differences may arise with alternative criteria that consider the bulk of the flow.

3.3. Eddy viscosity perturbation

In many studies that have examined the properties of the linearised Navier–Stokes equations, velocity perturbations resulting from optimal or stochastic forcing are computed by assuming that the turbulent viscosity distribution is not affected by the flow perturbation and follows an analytical or empirical distributions (Reynolds & Hussain 1972; del Álamo & Jiménez 2006; Hwang & Cossu 2010; Morra *et al.* 2019; Pickering *et al.* 2021). In the present case, and unlike previous work, the governing equations must include a transport equation for the turbulent viscosity. It is speculated that the peak location predicted by the present linear model (see figure 4) is determined in large part by the selectivity of the linearised Navier–Stokes operator, rather than by the specifics of the turbulence model adopted. However, the inclusion of such a model and the resulting perturbation of the turbulent viscosity $\nu_t^{(1)}$ is key to capture the influence of the heterogeneous surface roughness and the generation of secondary flows, as described in § 2.2. In practice, spanwise gradients of the eddy viscosity produce, through the QCR model, Reynolds stresses that act as source terms for the streamwise vorticity equation, resulting in secondary motions.

Figure 8 shows contours of the perturbation turbulent viscosity for several strip widths S . In figure 8(a), the QCR constant c_{r1} has been set to zero, to characterise the eddy viscosity distribution in the absence of cross-stream motions and highlight the interaction with the streamwise velocity fields of figure 6. In figure 8(b), the QCR constant is $c_{r1} = 0.3$. In general, positive eddy viscosity perturbations are observed above the high-roughness strips, and *vice versa*, reflecting the boundary condition (2.28) and the altered distance d from the wall. For narrow strips, the eddy viscosity perturbation is confined near the wall, given that rapid spatial variations of the eddy viscosity tend to be damped by the diffusion term in the linearised SA equation. As the strip gets wider, more-intense eddy

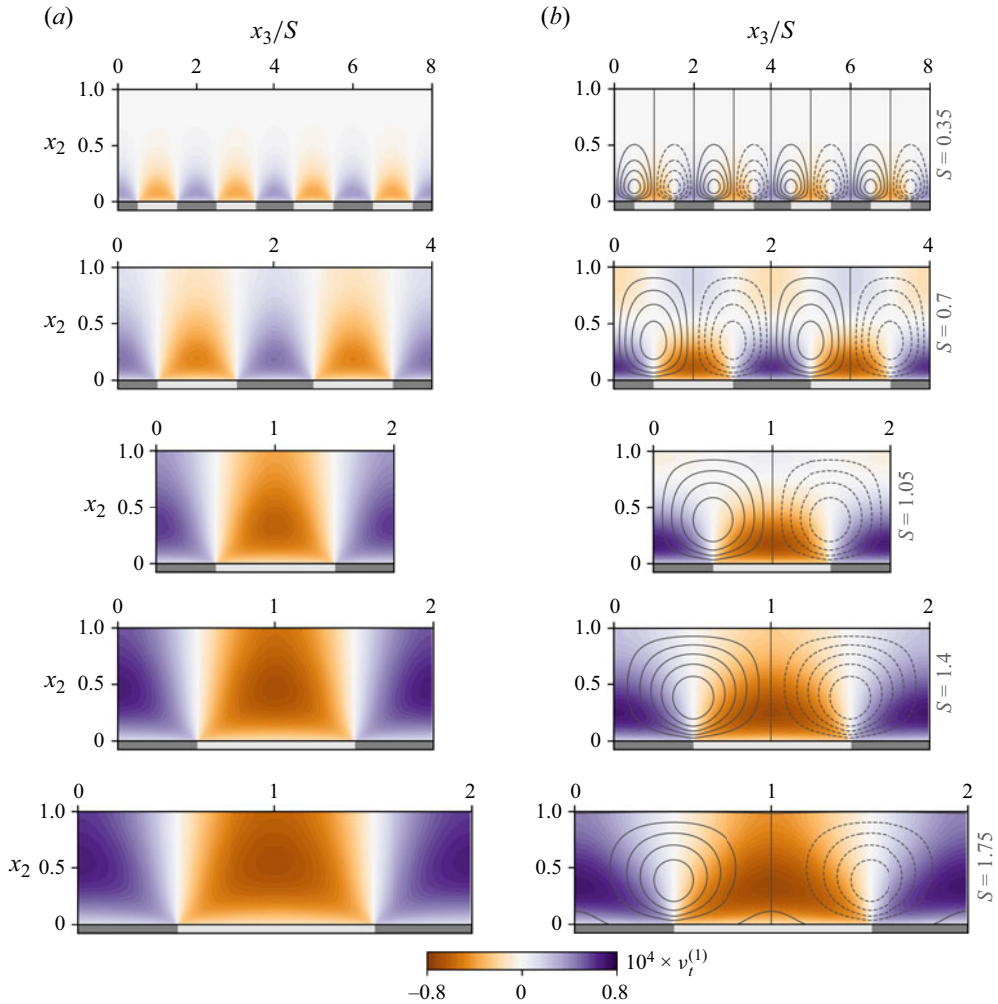


Figure 8. Contours of the eddy viscosity perturbation $v_t^{(1)}$ over roughness strips at $DC = 0.5$ for several strip widths S , without the QCR model (a) and with the QCR model (b). The field in the fundamental domain (see figure 1) is repeated four and two times for the two narrowest strip cases. Contour lines of the perturbation of the streamfunction $\psi^{(1)}$ are also reported to visualise the secondary flows. Negative $\psi^{(1)}$ contours are indicated by dashed lines. The Reynolds number is $Re_\tau = 1000$, for $k_s^{(0)} = 180$. The darker/lighter patches denote the location of the high-/low-roughness strips.

viscosity distributions are observed, reflecting the increased acceleration/deceleration of the flow over the low and high roughness strips, respectively. Small, but likely significant, changes are observed when secondary flows are ‘turned on’, see figure 8(b). It can be observed that the cross-stream motions produce a further distortion of the eddy viscosity distributions. This is the result of two mechanisms that result from the analysis of the SA transport model: (a) the advection of turbulent viscosity of the background flow operated by the vertical and lateral velocities and (b) the altered production of turbulent viscosity due to the alteration of wall-normal and spanwise gradients of the streamwise velocity.

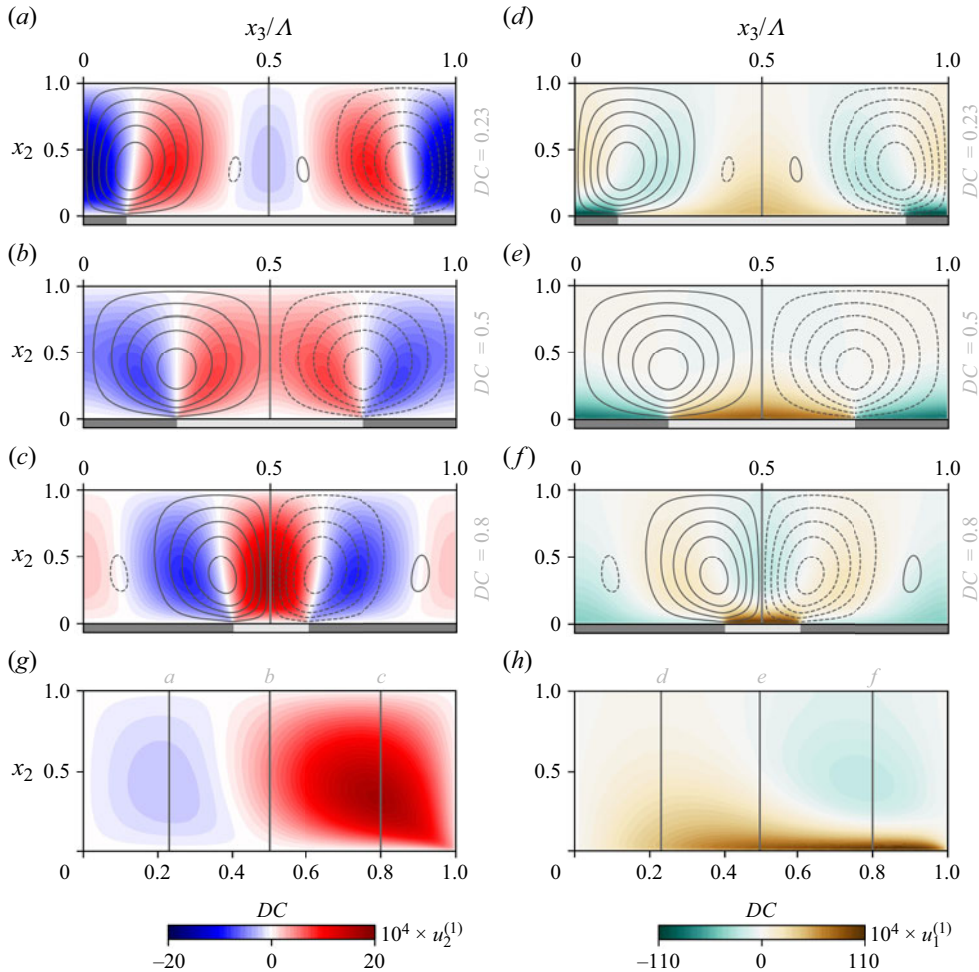


Figure 9. Contours of the wall-normal (a–c) and streamwise (d–f) velocity perturbation for increasing duty cycles, indicated in the figures, and $\Lambda = 2.8$. Panels (g) and (h) show the wall-normal and streamwise velocity, respectively, extracted on the vertical line (shown in panels a–f) at the centre of the low-roughness strip $x_3/\Lambda = 0.5$ for duty cycles ranging from 0 (narrow high-roughness strip) to 1 (wide high-roughness strips). The lines labelled (a)–(f) in panels (g) and (h) refer to the corresponding panels. The Reynolds number is $Re_\tau = 1000$ and $k_s^{(0)} = 180$.

3.4. Tertiary structures and role of the duty cycle

The present model shows that the duty-cycle appears to play an important role in controlling the formation of tertiary structures, which have so far not been observed for strip-type roughness (Neuhauser *et al.* 2022). This is shown in figure 9, where contours of the wall-normal and streamwise perturbation velocities are shown for increasing duty cycles, at $\Lambda = 2.8$. These cases correspond to the triangular marker in figure 4. For each of these solutions, as well as for other solutions in the interval $DC = [0, 1]$, the wall-normal and streamwise velocity profiles are extracted at the centre of the low-roughness strip. All these profiles are then combined together to form the colour map reported in the bottom panels of figure 9. This visualisation suggests that flow reversal over the low-roughness strip may begin to appear in practice as the duty cycle is decreased to about 0.4 and would

be the most intense for $DC \approx 0.23$ (i.e. for $S_h \approx 0.3S_l$). Incidentally, the occurrence of flow reversal and tertiary structures explains the two ‘ears’ of the contours of the kinetic energy density map of [figure 4\(a\)](#), where the cross-stream motions are relatively intense, compared to other duty cycles. This analysis also suggests that the vertical velocities over the low-roughness strip are most intense for a duty cycle equal to about 0.8 and not for the symmetric case $DC = 0.5$ which the kinetic energy density maps would suggest. Arguably, this can be attributed to the constructive interference of the wall-normal velocities induced by two neighbouring vortices, pushed closer to each other by the decreasing width of the low-roughness strip. The streamwise velocity field is also particularly affected by the duty cycle, as faster or slower flow over the low-roughness strip can be found depending on the DC . The transport of fast/slow fluid operated by the cross-stream velocities is particularly visible. For instance, for $DC = 0.23$ the left vortex, rotating counter-clockwise transports low-momentum fluid from the near-wall region at $x_3 = 0$ to its right flank, producing a negative velocity streak at $x_3 \approx 0.2$, and similarly for the other longitudinal vortex.

4. Generalising the framework to complex surface heterogeneities

It has been demonstrated that when conducting experiments ([Wangsawijaya et al. 2020](#)) or roughness-resolving simulations ([Stroh et al. 2020](#)) over realistic heterogeneous rough surfaces it is pivotal to ensure that the shear-increasing effects of roughness are decoupled from the inevitable variation of the mean surface height. Both roughness and elevation heterogeneity produce secondary currents and, therefore, the combination of such effects can have a significant influence on the strength and potentially the direction of the resulting secondary motions ([Schäfer et al. 2022](#); [Frohnepfel et al. 2024](#)). In this section, we analyse this aspect through the lens of the linearised model, to initiate the formulation of a unifying framework for flows over complex heterogeneous surfaces.

4.1. Secondary-flow-inducing source mechanisms

In the present linearised framework, in the limit case where the spanwise variation of the roughness or the elevation is small, ridge-type and strip-type roughness are modelled with the same approach. In both cases, the flow–surface interaction develops through three separate source mechanisms corresponding to three different inhomogeneous terms acting as forcing in the linearised equations. To illustrate these mechanisms, it is instructive to examine ridge-type roughness considered in our previous work ([Zampino et al. 2022](#)) where the mechanisms are all active. In such case, the lateral variation of the elevation was defined by a unitary peak-to-peak, zero-mean function $f(x_3)$ so that, e.g. the bottom wall of the channel is located at $x_2 = \epsilon f(x_3)$ and the small parameter ϵ controls the actual amplitude of the topography. The first source mechanism, denoted as A in what follows, is mediated by the linearised boundary condition on the streamwise velocity, e.g. on the lower wall,

$$u_1^{(1)}(x_2 = 0) = -f(x_3) \left. \frac{\partial u^{(0)}}{\partial x_2} \right|_{x_2=0} = -f(x_3) Re_\tau, \quad (4.1)$$

derived in [Zampino et al. \(2022\)](#). Physically, this condition produces a velocity slip that captures the acceleration and deceleration perceived by the bulk flow above the troughs and the crests of the non-planar topography, respectively. What leads to the formation of secondary flows is the resulting spanwise gradient of the streamwise velocity in the near-wall region. This gradient induce, via the QCR model, spanwise gradients of anisotropic Reynolds stresses (see [\(2.25\)](#)) that then create secondary flows.

This mechanism does not seem to have been discussed previously in the literature of secondary flows. More generally, we are not aware of studies that consider the somewhat artificial surface arrangement consisting of longitudinal, flush-mounted belts moving upstream/downstream alternated with regions of solid wall. This set-up would capture source mechanism *A* directly, and we predict that it could generate relatively intense secondary currents with a downwelling over the upstream-moving belts. When modelling strip-type roughness, this source mechanisms is not active since no-slip boundary conditions for the streamwise velocity are used. This is equivalent to stating that the mean height of the two roughness strips is the same and the boundary of the numerical domain is at some suitable location where the strip-averaged streamwise velocity goes to zero.

The second source mechanism, denoted as *B*, is active for both types of heterogeneity. It is mediated by the destruction term of the SA transport equation, where the inverse of the squared distance d between a point in the numerical domain and the nearest ‘wall’ models the blocking effect of the wall (Spalart & Allmaras 1994; Aupoix & Spalart 2003). With such term, the SA model predicts an accurate log-layer and, thus, lateral perturbations of the distance d induced by the elevation (via the function $f(x_3)$) or by the displacement of the virtual origin (via the term $d_0^{(1)}(x_3)$), produce a perturbation of the log-layer and spanwise gradients of the turbulent viscosity field. Crucially, the sign of this source mechanism is opposite for strip-type and ridge-type roughness: while locally increasing elevations correspond to locally reducing distances d , increasing roughness produces increasing distances, as the virtual origin is further displaced downwards beneath the boundary of the numerical domain. In this regard, the framework suggests that the mean roughness height is not the important factor. Rather, the displacement of the virtual origin, a dynamic parameter that ultimately depends on the drag of the surface, is what controls the intensity of the forcing and of the resulting secondary flows. As a side note, while source mechanism *A* acts as a boundary condition, source mechanism *B* acts at all wall distances, as it captures the perturbed development of the wall-bounded flow from a different origin.

The third source mechanism, denoted as *B'*, is again active for both types of heterogeneities. It is mediated by the inhomogeneous boundary condition on the modified turbulent viscosity. For ridge-type roughness, this is

$$\tilde{\nu}^{(1)}(x_2 = 0) = -f(x_3) \left. \frac{\partial \tilde{\nu}^{(0)}}{\partial x_2} \right|_{x_2=0} = -f(x_3)\kappa. \quad (4.2)$$

For strip-type roughness, the lateral variation of the virtual origin $d_0^{(1)}(x_3)$ plays the same role of the function $f(x_3)$ describing the ridge topography, but with an opposite effect as dictated by the boundary condition (2.28). This condition must be applied consistently with source mechanism *B*, so that the shifted eddy viscosity profile produced by such mechanism is consistent with the boundary condition (4.2). Studies on modelling roughness in RANS simulations (Aupoix & Spalart 2003) have shown (and we confirm it later) that this third mechanism is quite weak, because capturing the overall development of the turbulent structure from a different virtual origin is more important than applying non-zero boundary conditions for the turbulent quantities.

4.2. Combining elevation and roughness variations

To examine the relative strength and the combination of these three source mechanisms, we first perform linearised calculations for $Re_\tau = 1000$ for a smooth sinusoidal wall where

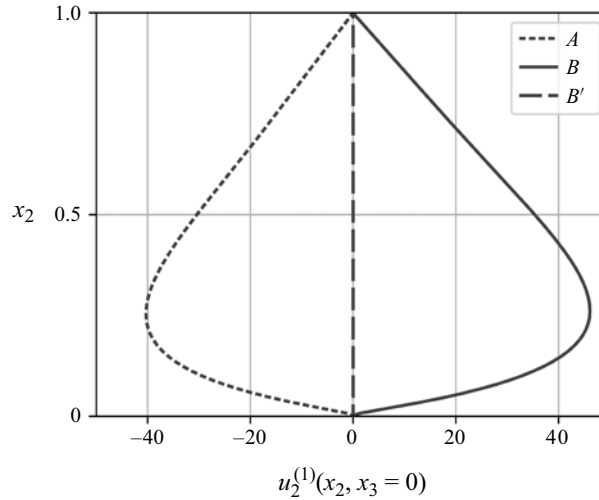


Figure 10. Wall-normal velocity profiles over the crest of a sinusoidal topography, for $\Lambda = 1$ and $Re_\tau = 1000$, obtained by activating each of the three secondary-flow-inducing source mechanisms in turn.

$f(x_3) = \cos(2\pi/\Lambda x_3)$, with period $\Lambda = 1$, by activating only one source mechanism each time. Results are reported in figure 10. The wall-normal velocity profiles, taken at $x_3 = 0$ over the crest of the topography, show that source mechanism A produces a downwelling flow over the region where the slip velocity is negative. Conversely, the decrease of the distance from the wall over the crest, source mechanism B , produces an upwelling of slightly greater magnitude, while source mechanism B' is much weaker than the first two, as discussed. Because the proposed model is linear, the superposition principle applies and the effect of varying simultaneously the roughness properties and the elevation can be obtained easily by combining appropriately solutions obtained in the two cases. For ridge-type roughness, source mechanisms A , B and B' are all active, while for strip-type roughness only source mechanisms B and B' should be retained, after inverting the sign of the induced flow given the different orientations of $f(x_3)$ and $d_0^{(1)}$ (see figure 12).

To better demonstrate the relative importance of these mechanisms, we then consider a configuration where strips and rectangular ridges are arranged in phase, and the high-roughness regions are placed over the ridges (see figure 11). The width S_l coincides with the gap between the ridges while S_h coincides with the ridge width (denoted as G and W in Zampino *et al.* 2022). To characterise the relative strength of the two effects, we introduce the parameter β as the ratio between the displacement of the virtual origin produced by the strips and the topography, so that

$$d_0^{(1)}(x_3) = \beta f(x_3), \quad (4.3)$$

with the caveat that positive displacements are in different directions depending on the type of heterogeneity. Case $\beta = 0$ corresponds to smooth ridges, leading to secondary flows produced by lateral variations of the elevation. As discussed in Zampino *et al.* (2022), the linearised RANS model predicts an upwelling over the high-elevation regions. On the other hand, case $\beta = 1$ corresponds to the combination of the two roughness heterogeneities where the downward displacement of the virtual origin produced by the shear-increasing roughness is, in theory, fully compensated by a increased elevation.

Figure 12 shows results of this analysis, where we conduct calculations over surfaces with combined roughness and elevation as a function of β . The kinetic energy density

Linear models of strip-type roughness

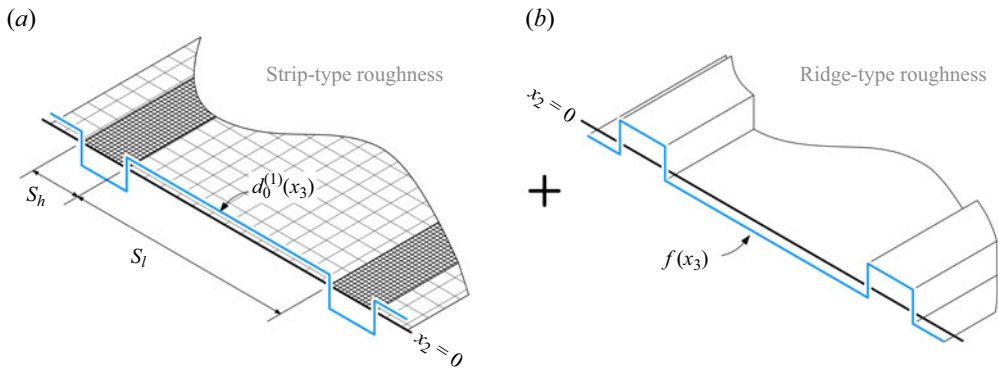


Figure 11. Superposition of high- and low-roughness strips with smooth rectangular ridges modelling the effect of lateral variation of elevation over the bottom wall of the channel. The lateral variation of the virtual origin of the rough surface is captured by $d_0^{(1)}(x_3)$ (positive if the virtual origin is below the mean height at $x_2 = 0$), while the lateral variation of the elevation is captured by the function $f(x_3)$ (positive if it is above $x_2 = 0$).

obtained at each composite surface is normalised with the reference value at $\beta = 0$ and is shown in figure 12(g). Results are shown for $Re_\tau = 1000$ and $k_s^{(0)} = 180$, for strip (and ridge) widths configurations characterised by constant $S_h = S_l = 0.7$. The kinetic energy shows a minimum for $\beta \approx 0.3$, where the cross-stream velocity components vanish and no secondary flows are predicted. The location of the minimum does not seem to depend greatly on the strip configuration (not shown for brevity). For $\beta > 0.3$ the effect of the lateral variation of the roughness becomes dominant and the associated kinetic energy density can be several times higher than the reference value. The resulting flow structure as β is increased, i.e. as the effect of roughness is increased, is shown in figures 12(a–f). Maps of the perturbation streamwise and wall-normal velocity components are shown, for $\beta = 0$, in the region where the ridge-type roughness is dominant, $\beta = 0.45$ close to the minimum of $\mathcal{K}(\beta)/\mathcal{K}(0)$, and 1, where the strip-type roughness is dominant. For $\beta = 0$ (figure 12a,d), the flow topology shows an upwelling over the ridges, as the upward displacement of the wall produced by the ridge-type roughness in this region is dominant. For $\beta = 0.45$ (figure 12b,e), secondary currents have changed in direction but their strength is relatively weak. For $\beta = 1$ (figure 12c,f), the flow topology shows a downwelling over the high-roughness strip, as the effect of the downward displacement of the virtual origin produced by the roughness prevails in this region over the influence of the increased elevation.

The key result of this analysis is that lateral variations of the roughness properties and of the elevation do not have the same effect on the strength of the resulting secondary motions, because of the ‘damping’ effect of the spanwise variation of the slip velocity produced by source mechanism A, active for heterogeneous elevation but not for heterogeneous roughness. The location of the minimum of $\mathcal{K}(\beta)$ suggests that the secondary-flow-inducing effect of roughness is about three times stronger than that of ridges, for the same displacement of the virtual origin in absolute terms. However, this prediction is clearly no better than the prediction of the strength of secondary flows for the two heterogeneities. The comparison with the heterogeneous roughness simulations of Chung *et al.* (2018) reported earlier suggests that the linear model captures quite well the strength of secondary motions over such surfaces. However, for ridges, recent work (Castro & Kim 2024) has suggested that the linear model over-predicts the intensity of

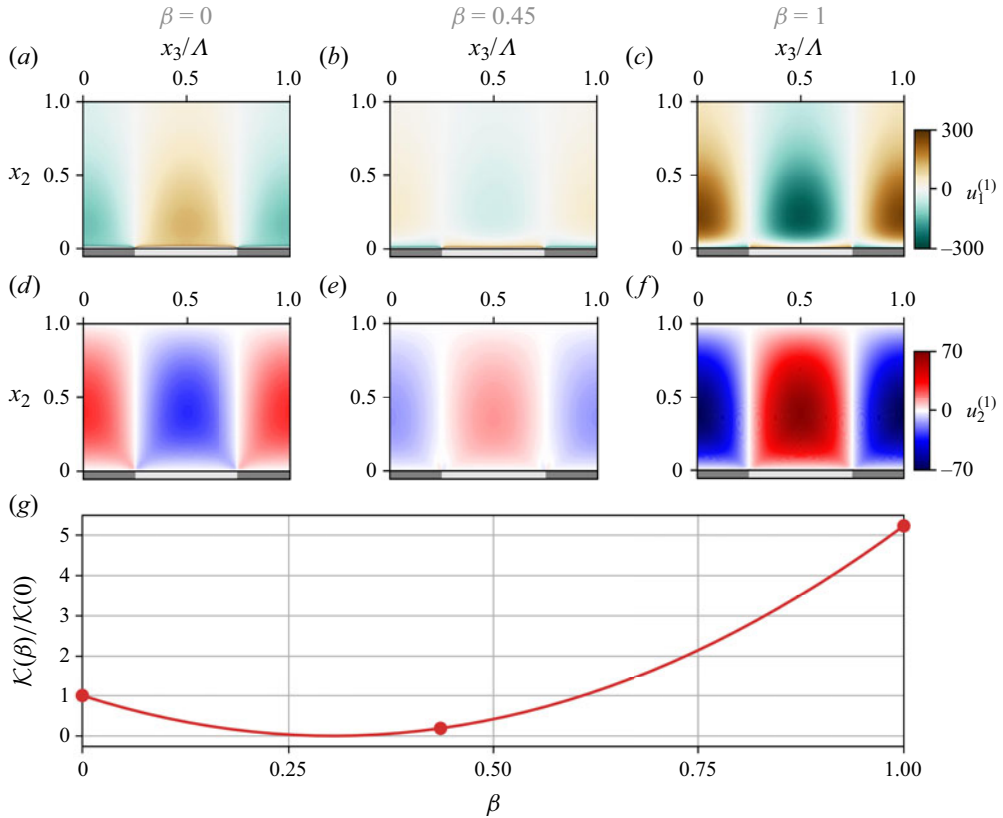


Figure 12. Contours of the perturbation streamwise (a – c) and wall-normal (d – f) velocity components for combinations of ridge-type and strip-type roughness for $S_h = S_l = 0.7$. The parameter β is 0.0, 0.45 and 1, as we move from left to right with configurations where the effect of the elevation heterogeneity dominates to cases where the roughness heterogeneity prevails. Normalised kinetic energy density of the combination of both ridge-type and strip-type roughness as a function of the parameter β (f). The Reynolds number is fixed at 1000 and $k_s^{(0)} = 180$.

secondary motion for tall ridges, owing to the importance of nonlinear effects near the corners of the ridges, while predictions can be more accurate for short ridges that do not protrude excessively in the wall-bounded flow. Overall, this indicates that the response of the wall-bounded flow to a perturbation of the surface elevation is far from being linear. To the best of the authors' knowledge, evidence for this claim was perhaps first given in Wang & Cheng (2006) (see their figure 20), who showed how the vertical velocity produced by secondary motions saturates rather quickly as the height of the topography is increased. This last piece of evidence suggests that the secondary-flow-inducing effect of the roughness might be even stronger than what the linear model suggest here, although a precise quantification might require dedicated experimental work. Overall, this could also justify the recent results of Frohnäpfel *et al.* (2024) who considered the same surface arrangement considered in this section, with roughness strips located in phase with the ridges. These authors increased the ridge height but did not observe a reversal of the flow direction above the ridges, which was dominated by the downwelling caused by the roughness. Using their data, we calculate the height of the ridges to be 5.16 % the height of the channel and the downward displacement of the virtual origin to be 1.08 %, from their homogeneous roughness data, for a ratio $\beta \simeq 0.21$. This ratio is clearly to the left of the

minimum in [figure 12](#), reinforcing the idea that the response of the wall-bounded flow to finite lateral variations of the elevation are less intense than predicted by a linear model for infinitesimal perturbations.

5. Discussion and concluding remarks

In this paper, we proposed a linearised RANS-based framework to predict the structure of Prandtl's secondary flows of the second kind developing over laterally heterogeneous rough surfaces. The work extends our previous efforts on modelling smooth non-planar surfaces ([Zampino *et al.* 2022](#)), e.g. surfaces with longitudinal ridges. The model couples the linearised RANS equations with the SA transport equation to capture the altered turbulent structure. Rough surfaces with alternating streamwise-aligned strips of high and low roughness are modelled using established RANS modelling strategies available in the literature for homogeneous rough surfaces ([Aupoix 2007](#)). Briefly, these strategies adopt a virtual origin framework, whereby the shift of the logarithmic profile is obtained by displacing beneath the boundary of the numerical domain the origin from which turbulent quantities develop ([Rotta 1962](#)). This results in altered boundary conditions as well as a domain forcing term when the distance from the wall appears in the turbulence model's transport equations. The framework also employs a nonlinear Reynolds stress model, i.e. the QCR (see [Spalart 2000](#)), so that secondary currents induced by the inhomogeneity of anisotropic turbulent stresses can be predicted ([Speziale 1982](#)).

There are several aspects that the model predicts remarkably well in agreement with previous observations. One first aspect is the presence of three separate flow regimes as the strip width is increased ([Chung *et al.* 2018](#)). For narrow strips, the linear model supports a flow structure consisting of rolls localised in the vicinity of the wall and having wall-normal size scaling linearly with the strip width. For wider strips, the flow structure tends to an 'isolated-vortex' regime, where streamwise vorticity is concentrated in a roughly square region localised around the transition between strips, while the bulk flow in the centre of the roughness strips tends to its homogeneous rough-wall flow dictated by the local roughness properties. In the intermediate regime, secondary currents are most intense when the high- and low-roughness strips have the same widths, and are equal to about 0.7 of the half-channel height. The model also provides adequate quantitative predictions of the intensity of the cross-stream velocity component, compared with, e.g. the numerical simulations of ([Chung *et al.* 2018](#)). A second aspect concerns tertiary structures and flow reversal, not observed in previous studies on roughness strips that have most often examined high- and low-roughness strips of equal width. The linear model predicts that these phenomena only appear when the strips have different width. For instance, for $\Delta = 2.8$, flow reversal is strongest on the low-roughness strip when this strip is about four times wider than the high-roughness strip. It would be interesting to confirm this prediction through experiments or simulations. A third aspect concerns the occurrence of low- and high-momentum pathways flanking the longitudinal rolls, where high-speed flow may be found on the high-roughness strip (and *vice versa*) in regions dominated by the vertical velocities induced by the rolls. Away from the rolls, or for wide strips, the expected relationship between surface roughness and streamwise velocity defect is recovered.

From a practical standpoint, the advantage of the present approach is, undoubtedly, its computational efficiency. However, the ability to rapidly probe the parameter space has enabled progress to be made on a more fundamental standpoint. Specifically, previous work has suggested that secondary currents may be the time-averaged picture of naturally occurring large-scale motions locked in place by the heterogeneity. The robustness of

the above-mentioned similarities between the flow structure predicted by the present framework and previous observations suggests an alternative input–output perspective whereby these currents are the output response of the Navier–Stokes operator linearised about the turbulent mean and subjected of a steady, streamwise-independent forcing localised at the wall, associated to the lateral perturbation of the surface characteristics. This perspective complements the well-accepted viewpoint that instantaneous coherent structures in wall-bounded turbulence may be described to a satisfactory degree by the output properties of the linearised operator subjected to a random forcing (Hwang & Cossu 2010; McKeon & Sharma 2010). Admittedly, this viewpoint does not explain the observed interplay between large-scale motions and secondary structures (Wangsawijaya & Hutchins 2022), whereby energy of the former leeches into the latter. One possible explanation that is worth exploring further is that the mean flow distortion produced by the secondary currents may locally alter the selective amplification properties of the linearised operator, producing a spanwise modulation of the nature of large-scale motions that may be interpreted as an energy interaction between secondary currents and large-scale motions.

A second key output of this study is that it offers a unified perspective to examine both ridge-type and strip-type roughness. Examination of these two cases within the present framework shows that secondary motions produced by complex surface heterogeneities, e.g. arbitrary combinations of elevation and roughness properties, may be seen as originating from two separate source mechanisms. The first is a lateral variation of the virtual origin from which the mean turbulence structure develops. The sign of this variation is opposite for ridge-type and strip-type roughness: the virtual origin is shifted upwards by ridges, and downwards by higher roughness. The second source mechanism is mediated by the lateral variation of the streamwise slip velocity in the vicinity of the wall, and the associated spanwise gradients of the streamwise velocity. This source mechanism captures the acceleration/deceleration perceived by the bulk flow above the troughs and crests of a non-planar topography, respectively, or when the mean roughness height varies laterally. In ridge-type roughness, we have shown that this source mechanism damps the first so that the resulting secondary motions are weaker compared with those that would be predicted from the first mechanism. In other words, *for the same lateral variation of the virtual origin* strip-type roughness produces more intense secondary flows than ridge-type roughness. The caveat is that this perspective applies, in the limit where the lateral variation of surface attributes is ‘small’, in the region of validity of the linear model. For finite-amplitude perturbations of the surface attributes, these predictions would need to be further verified. In any case, the present modelling framework suggests that the mean roughness height, a geometric quantity used in previous studies that considered the coupling of roughness and elevation is not the important quantity to be monitored when investigating combinations of elevation and roughness. Instead, we suggest that the notion of the virtual origin, a dynamical parameter associated to the downward shift of the logarithmic distribution, should be considered.

Like all other analyses of the linearised Navier–Stokes operator, the present approach yields useful insight but has its limitations. The ability of a one-equation turbulence model equipped with a nonlinear Reynolds stress model to capture the unsteady motion of secondary structures may be questioned. A more extensive assessment of alternative turbulence modelling strategies and a comparison with high-fidelity simulations is certainly warranted in future work, although it must be pointed out that the SA-QCR model used here does seem to capture fairly well the anisotropic nature of the Reynolds stress tensor in square-duct flow (Modesti 2020). In this regard, it is speculated that such alternatives may not necessarily lead to significant qualitative changes in the predictions obtained here. In fact, we argue that the selectivity of the linearised Navier–Stokes

operator may be dominant, with minimal effects of the turbulence modelling strategy adopted. This speculation is supported by the extensive evidence that useful predictions have been made using linearised Navier–Stokes equation approaches using much simpler turbulence modelling techniques than used here. Such a speculation may be verified simply by examining the response obtained from other turbulence modelling strategies. Given that linearisation of complex models is a tedious task, nonlinear calculations using existing solvers may be performed for sufficiently small roughness variations that the linear approximation is reasonably valid. A further limitation is that it is unclear how sensible is the streamwise independence assumption used here when secondary motions display a strong meandering behaviour (Kevin *et al.* 2019).




Further, the importance of nonlinear effects neglected in the present linear framework in altering the structure of secondary flows is not clearly understood. Convergence of the expansion (2.21) for finite-amplitude surface perturbations should be examined. Analyses of the streamwise vorticity budget for ridge-type roughness (Castro & Kim 2024) shows that nonlinear effects appear significant near sharp geometric features, and similar conclusions might apply to regions where roughness properties vary sharply. Nonlinear effects must also be introduced in order to predict the change in drag (Zampino 2023), since the one further limitation of the present linear approach is that it offers no insight into the dependence of drag on the surface properties. This would be highly useful for predicting the drag of real-world surfaces, which is currently a topic of active research. Clearly, the question is whether classical turbulence models and established rough-wall treatment strategies may adequately capture the drag characteristics of heterogeneous surfaces. A possible avenue forward would be to bypass these modelling strategies and the small-amplitude assumption and instead adopt the framework reviewed in Zare, Georgiou & Jovanović (2020) to model the second-order statistics of the velocity fluctuations from the response of the linearised Navier–Stokes subjected to a structured stochastic forcing. However, the extension of this framework to rough surfaces would need to be considered first.

Acknowledgements. We acknowledge funding from the EPSRC (grant reference EP/V00199X/1). We are grateful for the insightful discussions with Professor Ian Castro and Professor Jae-Wook Kim.

Declaration of interests. The authors report no conflict of interest.

Data access statement. All data supporting this study will be openly available from the University of Southampton repository.

Author ORCIDs.

-  D. Lasagna <https://orcid.org/0000-0002-6501-6041>;
-  G. Zampino <https://orcid.org/0000-0002-5730-4430>;
-  B. Ganapathisubramani <https://orcid.org/0000-0001-9817-0486>.

Appendix A. Linearisation of the normalised rotation tensor

The normalised rotation tensors at order zero and order one are

$$O^{(0)} = \begin{bmatrix} 0 & \text{sign}(\Gamma) & 0 \\ -\text{sign}(\Gamma) & 0 & 0 \\ 0 & 0 & 0 \end{bmatrix}, \quad (\text{A1})$$

$$O^{(1)} = \begin{bmatrix} 0 & 0 & \frac{\text{sign}(\Gamma)}{\Gamma} \frac{\partial u_1^{(1)}}{\partial x_3} \\ 0 & 0 & \frac{\text{sign}(\Gamma)}{\Gamma} \left(\frac{\partial u_2^{(1)}}{\partial x_3} - \frac{\partial u_3^{(1)}}{\partial x_2} \right) \\ -\frac{\text{sign}(\Gamma)}{\Gamma} \frac{\partial u_1^{(1)}}{\partial x_3} & -\frac{\text{sign}(\Gamma)}{\Gamma} \left(\frac{\partial u_2^{(1)}}{\partial x_3} - \frac{\partial u_3^{(1)}}{\partial x_2} \right) & 0 \end{bmatrix}, \quad (A2)$$

where Γ is the zero-order wall-normal gradient of the streamwise velocity and sign is the sign function.

REFERENCES

- DEL ÁLAMO, J.C. & JIMÉNEZ, J. 2006 Linear energy amplification in turbulent channels. *J. Fluid Mech.* **559**, 205–213.
- ANDERSON, W., BARROS, J.M., CHRISTENSEN, K.T. & AWASTHI, A. 2015 Numerical and experimental study of mechanisms responsible for turbulent secondary flows in boundary layer flows over spanwise heterogeneous roughness. *J. Fluid Mech.* **768**, 316–347.
- AUPOIX, B. 2007 A general strategy to extend turbulence models to rough surfaces: application to Smith's k - L model. *J. Fluids Engng* **129** (10), 1245–1254.
- AUPOIX, B. & SPALART, P.R. 2003 Extensions of the Spalart–Allmaras turbulence model to account for wall roughness. *Intl J. Heat Fluid Flow* **24**, 454–462.
- BAI, H.L., KEVIN, HUTCHINS, H. & MONTY, J.P. 2018 Turbulence modifications in a turbulent boundary layer over a rough wall with spanwise-alternating roughness strips. *Phys. Fluid* **30** (5), 055105.
- BARROS, J.M. & CHRISTENSEN, K.T. 2014 Observation of turbulent secondary flows in a rough-wall boundary layer. *J. Fluid Mech.* **748**, R1.
- BOTTARO, A., SOUEID, H. & GALLETTI, B. 2006 Formation of secondary vortices in turbulent square-duct flow. *AIAA J.* **44**, 803–811.
- BOU-ZEID, E., PARLANGE, M.B. & MENEVEAU, C. 2007 On the parameterization of surface roughness at regional scales. *J. Atmos. Sci.* **64** (1), 216–227.
- BRANDT, L. 2014 The lift-up effect: the linear mechanism behind transition and turbulence in shear flows. *Eur. J. Mech. B Fluids* **47**, 80–96.
- BRERETON, G.J. & YUAN, J. 2018 Wall-roughness eddy viscosity for Reynolds-averaged closures. *Intl J. Heat Fluid Flow* **73**, 74–81.
- CASTRO, I.P. & KIM, J.W. 2024 Secondary motions in turbulent ribbed channel flows. *J. Fluid Mech.* **988**, A2.
- CASTRO, I.P., KIM, J.W., STROH, A. & LIM, H.C. 2021 Channel flow with large longitudinal ribs. *J. Fluid Mech.* **915**, A92.
- CHAVARIN, A. & LUHAR, M. 2020 Resolvent analysis for turbulent channel flow with riblets. *AIAA J.* **58** (2), 589–599.
- CHEN, W.L., LIEN, F.S. & LESCHZNER, M.A. 1997 Non-linear eddy-viscosity modelling of transitional boundary layers pertinent to turbomachine aerodynamics. *Intl J. Heat Fluid Flow* **19**, 297–306.
- CHERNYSHENKO, S.I. & BAIG, M.F. 2005 The mechanism of streak formation in near-wall turbulence. *J. Fluid Mech.* **544**, 99–131.
- CHUNG, D., MONTY, J.P. & HUTCHINS, N. 2018 Similarity and structure of wall turbulence with lateral wall shear stress variations. *J. Fluid Mech.* **847**, 591–613.
- COSSU, C., PUJALS, G. & DEPARDON, S. 2009 Optimal transient growth and very large-scale structures in turbulent boundary layers. *J. Fluid Mech.* **619**, 79–94.
- DURBIN, P.A., MEDIC, G., SEO, J.-M., EATON, J.K. & SONG, S. 2000 Rough wall modification of two-layer $\kappa - \epsilon$. *J. Fluids Eng.* **123**, 16–21.
- FOROOGHI, P., YANG, X.I.A. & ABKAR, M. 2020 Roughness-induced secondary flows in stably stratified turbulent boundary layers. *Phys. Fluids* **32** (10), 105118.

- FROHNAPFEL, B., VON DEYN, L., YANG, J., NEUHAUSER, J., STROH, A., ÓRLÚ, R. & GATTI, D. 2024 Flow resistance over heterogeneous roughness made of spanwise-alternating sandpaper strips. *J. Fluid Mech.* **980**, A31.
- GOLDSTEIN, D.B. & TUAN, T.-C. 1998 Secondary flows induced by riblets. *J. Fluid Mech.* **363**, 115–151.
- GRIGSON, C. 1992 Drag losses of new ships caused by hull finish. *J. Ship Res.* **36**, 182–196.
- HERRING, H.J. & MELLOR, G.L. 1968 A method of calculating compressible turbulent boundary layers. *Tech. Rep.* 19680025624. NASA Contractor Report.
- HINZE, J.O. 1973 Experimental investigation on secondary currents in the turbulent flow throughout a straight conduit. *Appl. Sci. Res.* **28** (9), 453–465.
- HUTCHINS, N., GANAPATHISUBRAMANI, B., SCHULTZ, M.P. & PULLIN, D.I. 2023 Defining an equivalent homogeneous roughness length for turbulent boundary layers developing over patchy or heterogeneous surfaces. *Ocean Engng* **271**, 113454.
- HWANG, H.G. & LEE, J.H. 2018 Secondary flows in turbulent boundary layers over longitudinal surface roughness. *Phys. Rev. Fluids* **3**, 014608.
- HWANG, Y. & COSSU, C. 2010 Linear non-normal energy amplification of harmonic and stochastic forcing in the turbulent channel flow. *J. Fluid Mech.* **664**, 51–73.
- JIMÉNEZ, J. 2004 Turbulent flows over rough walls. *Annu. Rev. Fluid Mech.* **36**, 173–196.
- KEVIN, K., MONTY, J. & HUTCHINS, N. 2019 The meandering behaviour of large-scale structures in turbulent boundary layers. *J. Fluid Mech.* **865**, R1.
- KNOLL, D.A. & KEYES, D.E. 2004 Jacobian-free Newton–Krylov methods: a survey of approaches and applications. *J. Comput. Phys.* **193**, 357–397.
- LEE, J.H., SUNG, H.J. & ADRIAN, R.J. 2019 Space–time formation of very-large-scale motions in turbulent pipe flow. *J. Fluid Mech.* **881**, 1010–1047.
- LONG, Y., WANG, J. & PAN, C. 2023 The influence of roughness-element-spacing on turbulent entrainment over spanwise heterogeneous roughness. *Phys. Fluids* **35** (8), 085127.
- LUHAR, M., SHARMA, A.S. & MCKEON, B.J. 2015 A framework for studying the effect of compliant surfaces on wall turbulence. *J. Fluid Mech.* **768**, 415–441.
- MCKEON, B.J. & SHARMA, A.S. 2010 A critical-layer framework for turbulent pipe flow. *J. Fluid Mech.* **658**, 336–382.
- MEDJNOUN, T., VANDERWEL, C. & GANAPATHISUBRAMANI, B. 2018 Characteristics of turbulent boundary layers over smooth surfaces with spanwise heterogeneities. *J. Fluid Mech.* **838**, 516–543.
- MEDJNOUN, T., VANDERWEL, C. & GANAPATHISUBRAMANI, B. 2020 Effects of heterogeneous surface geometry on secondary flows in turbulent boundary layers. *J. Fluid Mech.* **886**, A31.
- MEJIA-ALVAREZ, R. & CHRISTENSEN, K. 2013 Wall-parallel stereo particle-image velocimetry measurements in the roughness sublayer of turbulent flow overlying highly irregular roughness. *Phy. Fluids* **25**, 015106.
- MEYERS, J., GANAPATHISUBRAMANI, B. & CAL, R.B. 2019 On the decay of dispersive motions in the outer region of rough-wall boundary layers. *J. Fluid Mech.* **862**, R5.
- MOARREF, R. & JOVANOVIĆ, M.R. 2012 Model-based design of transverse wall oscillations for turbulent drag reduction. *J. Fluid Mech.* **707**, 205–240.
- MODESTI, D. 2020 A priori tests of eddy viscosity models in square duct flow. *Theor. Comput. Fluid Dyn.* **34** (5), 713–734.
- MORRA, P., SEMERARO, O., HENNINGSON, D.S. & COSSU, C. 2019 On the relevance of Reynolds stresses in resolvent analyses of turbulent wall-bounded flows. *J. Fluid Mech.* **867**, 969–984.
- NEUHAUSER, J., SCHÄFER, K., GATTI, D. & FROHNAPFEL, B. 2022 Simulation of turbulent flow over roughness strips. *J. Fluid Mech.* **945**, A14.
- PERKINS, H.J. 1970 The formation of streamwise vorticity in turbulent flow. *J. Fluid Mech.* **44**, 721–740.
- PICKERING, E., RIGAS, G., SCHMIDT, O.T., SIPP, D. & COLONIUS, T. 2021 Optimal eddy viscosity for resolvent-based models of coherent structures in turbulent jets. *J. Fluid Mech.* **917**, A29.
- PRAKASH, A. & LAURENDEAU, E. 2020 Consistent surface roughness extension for wall functions. *Intl J. Heat Fluid Flow* **82**, 108552.
- PRANDTL, L. 1952 *Essentials of Fluid Dynamics*. Hafner.
- PUJALS, G., GARCÍA-VILLALBA, M., COSSU, C. & DEPARDON, S. 2009 A note on optimal transient growth in turbulent channel flows. *Phys. Fluids* **21**, 015109.
- RAN, W., ZARE, A. & JOVANOVIĆ, M.R. 2020 Model-based design of riblets for turbulent drag reduction. *J. Fluid Mech.* **906**, A7.
- REYNOLDS, W.C. & HUSSAIN, A.K.M.F. 1972 The mechanism of an organized wave in turbulent shear flow. Part 3. Theoretical models and comparisons with experiments. *J. Fluid Mech.* **54**, 263–288.
- ROTTA, J.C. 1962 Turbulent boundary layers in incompressible flow. *Prog. Aerosp. Sci.* **2**, 1–95.

- SCHÄFER, K., STROH, A., FOROOGHI, P. & FROHNAPFEL, B. 2022 Modelling spanwise heterogeneous roughness through a parametric forcing approach. *J. Fluid Mech.* **930**, A7.
- SPALART, P.R. 2000 Strategies for turbulence modelling and simulations. *Intl J. Heat Fluid Flow* **21**, 252–263.
- SPALART, P.R. & ALLMARAS, S.R. 1994 A one-equation turbulence model for aerodynamic flows. *Rech. Aerosp.* **1**, 5–21.
- SPEZIALE, C.G. 1982 On turbulent secondary flows in pipes of noncircular cross-section. *Intl J. Engng Sci.* **20** (7), 863–872.
- SPEZIALE, C.G., SARKAR, S. & GATSKI, T.B. 1991 Modelling the pressure-strain correlation of turbulence: an invariant dynamical system approach. *J. Fluid Mech.* **227**, 254–272.
- STROH, A., HASEGAWA, Y., KRIEGSEIS, J. & FROHNAPFEL, B. 2016 Secondary vortices over surfaces with spanwise varying drag. *J. Turbul.* **17**, 1142–1158.
- STROH, A., SCHÄFER, K., FROHNAPFEL, B. & FOROOGHI, P. 2020 Rearrangement of secondary flow over spanwise heterogeneous roughness. *J. Fluid Mech.* **885**, R5.
- SUGA, K., CRAFT, T.J. & IACOVIDES, H. 2006 An analytical wall-function for turbulent flows and heat transfer over rough walls. *Intl J. Heat Fluid Flow* **27** (5), 852–866.
- TOWNSEND, A.A.R. 1976 *The Structure of Turbulent Shear Flow*. Cambridge University Press.
- VANDERWEL, C. & GANAPATHISUBRAMANI, B. 2015 Effects of spanwise spacing on large-scale secondary flows in rough-wall turbulent boundary layers. *J. Fluid Mech.* **774**, R2.
- VIDAL, A., NAGIB, H.M., SCHLATTER, P. & VINUESA, R. 2018 Secondary flow in spanwise-periodic in-phase sinusoidal channels. *J. Fluid Mech.* **851**, 288–316.
- VISWANATH, D. 2007 Recurrent motions within plane Couette turbulence. *J. Fluid Mech.* **580**, 339–358.
- WANG, Z.Q. & CHENG, N.S. 2006 Time-mean structure of secondary flows in open channel with longitudinal bedforms. *Adv. Water Resour.* **29**, 1634–1649.
- WANGSAWIJAYA, D.D., BAIDYA, R., CHUNG, D., MARUSIC, I. & HUTCHINS, N. 2020 The effect of spanwise wavelength of surface heterogeneity on turbulent secondary flows. *J. Fluid Mech.* **894**, A7.
- WANGSAWIJAYA, D.D. & HUTCHINS, N. 2022 Investigation of unsteady secondary flows and large-scale turbulence in heterogeneous turbulent boundary layers. *J. Fluid Mech.* **934**, A40.
- WILLINGHAM, D., ANDERSON, W., CHRISTENSEN, K.T. & BARROS, J.M. 2014 Turbulent boundary layer flow over transverse aerodynamic roughness transitions: induced mixing and flow characterization. *Phy. Fluids* **26**, 025111.
- YANG, J. & ANDERSON, W. 2018 Numerical study of turbulent channel flow over surfaces with variable spanwise heterogeneities: topographically-driven secondary flows affect outer-layer similarity of turbulent length scales. *Flow Turbul. Combust.* **100**, 1–17.
- ZAMPINO, G. 2023 Linearized Reynolds-averaged Navier–Stokes model for the prediction of secondary flows on heterogeneous surfaces. PhD thesis, University of Southampton.
- ZAMPINO, G., LASAGNA, D. & GANAPATHISUBRAMANI, B. 2022 Linearised Reynolds-averaged predictions of secondary currents in turbulent channels with topographic heterogeneity. *J. Fluid Mech.* **944**, A4.
- ZAMPINO, G., LASAGNA, D. & GANAPATHISUBRAMANI, B. 2023 Scaling of secondary flows with surface parameters: a linear approach. *Intl J. Heat Fluid Flow* **102**, 109148.
- ZAMPIRON, A., CAMERON, S. & NIKORA, V. 2020 Secondary currents and very-large-scale motions in open-channel flow over streamwise ridges. *J. Fluid Mech.* **887**, A17.
- ZAMPIRON, A., CAMERON, S. & NIKORA, V. 2021 Momentum and energy transfer in open-channel flow over streamwise ridges. *J. Fluid Mech.* **915**, A42.
- ZARE, A., GEORGIOU, T.T. & JOVANOVIĆ, M.R. 2020 Stochastic dynamical modeling of turbulent flows. *Annu. Rev. Control Robot. Auton. Syst.* **3** (1), 195–219.
- ZHDANOV, O., JELLY, T.O. & BUSSE, A. 2024 Influence of ridge spacing, ridge width, and Reynolds number on secondary currents in turbulent channel flow over triangular ridges. *Flow Turbul. Combust.* **112** (1), 105–128.